Chemical Science

ROYAL SOCIETY OF CHEMISTRY

REVIEW

View Article Online
View Journal | View Issue

Cite this: *Chem. Sci.*, 2026, **17**, 118

Crystallization regulation of solution-processed metal halide perovskite light-emitting diodes

Long-Xue Cao,†[a] Yu-Hang Zhang,†[a] Yang Shen,*[ac] Yan-Qing Li*[b] and Jian-Xin Tang *[ac]

Perovskite Light-Emitting Diodes (PeLEDs) hold significant promise for future applications in displays due to their exceptional optoelectronic properties. However, the complexity of the crystallization process during the preparation of metal halide perovskite often leads to morphological inhomogeneity, defect-mediated non-radiative recombination losses, and subsequent performance degradation in devices. A profound understanding of perovskite nucleation and crystallization dynamics is crucial for fabricating high-performance PeLEDs. Based on this premise, this review systematically summarizes advanced strategies for regulating perovskite crystallization kinetics, which are grouped into two approaches: regulating nucleation sites to achieve dense and uniform perovskite films, and delaying crystal growth to enlarge grain size and suppress defect-mediated non-radiative recombination losses. In addition, this review examines the current challenges facing future full-color displays and large-scale production in PeLEDs. Finally, we outline promising future research directions, including the development of machine learning, and scalable fabrication techniques such as blade coating and inkjet printing, to bridge the gap between laboratory research and commercial applications. This review aims to provide comprehensive theoretical and practical insights into perovskite crystallization optimization, thereby accelerating the commercialization of PeLED technology.

Received 16th September 2025
Accepted 28th November 2025

DOI: 10.1039/d5sc07163a

rsc.li/chemical-science

1 Introduction

Solution-processed metal halide perovskites exhibit significant advantages, including tunable optical bandgaps, low manufacturing costs, superior charge transport properties, and high color purity.[1–6] These intrinsic characteristics make perovskites highly promising for integration into light-emitting diode (LED) displays, advancing next-generation display technologies that meet the stringent BT.2020 standard.[7–12] Rapid process has been made in recent years to achieve high efficiency

[a]*Institute of Functional Nano & Soft Materials (FUNSOM), Soochow University, Suzhou 215123, China. E-mail: yangshen@suda.edu.cn; jxtang@suda.edu.cn*
[b]*School of Physics and Electronic Science, East China Normal University, Shanghai, 200062, China. E-mail: yqli@phy.ecnu.edu.cn*
[c]*Macao Institute of Materials Science and Engineering (MIMSE), Macau University of Science and Technology, Taipa 999078, Macau, China*
† These authors contributed equally to this work.

Long-Xue Cao

Long-Xue Cao received her MSc (2023) degree in physics from Liaocheng University. Now, she is a PhD candidate in physics under the supervision of Prof. Jian-Xin Tang at the Institute of Functional Nano & Soft Materials (FUNSOM) of Soochow University. Her research interests lie in crystallization regulation and interfacial engineering of solution-processed metal halide perovskite light-emitting diodes.

Yu-Hang Zhang

Yu-Hang Zhang received his B.E. degree from Henan University of Science and Technology in 2023. He is now an M.S. candidate at FUNSOM, Soochow University, supervised by Prof. Jian-Xin Tang. His research focuses on perovskite crystallization control and perovskite-organic tandem light-emitting diodes.

PeLEDs.[13–16] The preparation of high-quality perovskite films with high crystallinity and low defect density can achieve performance metrics comparable to commercial organic LEDs (OLEDs).[17–23] Indeed, high-quality perovskite displays integrated on thin-film transistor (TFT) substrates have been demonstrated in recent studies, indicating the potential of perovskite-based LEDs to become the next generation of display technologies.[8–10,24,25] However, the complex crystallization process during perovskite growth introduces numerous variables, posing challenges to the study of key scientific issues and limiting the development of PeLEDs.[26–28] The inherent complexity stems from the sensitivity of perovskite crystallization to a wide range of factors, including interfacial energetics, precursor composition, solvent coordination, ambient atmosphere, and annealing temperature. These factors collectively influence nucleation density, crystal growth rate, phase purity, and ultimately the morphological and optoelectronic quality of the resulting films. Uncontrolled crystallization often leads to heterogeneous films with defects such as pinholes, and incomplete surface coverage, which act as non-radiative recombination centers and impede efficient charge transport. Precise crystallization management enables the formation of uniform, pinhole-free perovskite films with low defect densities, which are essential for enhancing charge injection, reducing efficiency roll-off, and improving operational stability. Therefore, understanding and controlling the crystallization kinetics of perovskites are therefore critical for achieving high-quality perovskite-based displays.

Although substantial research has been devoted to understanding the fundamental theories of perovskite nucleation and growth, there remains a lack of systematic guidance in translating these theoretical principles into effective crystallization regulation strategies. This review proposes decoupling the crystallization process into two distinct yet synergistic regulatory dimensions: precise control of nucleation sites and directed retardation of crystal growth. Within this framework, we systematically summarize advanced strategies for modulating perovskite crystallization kinetics. Specifically, we explore the impact of perovskite crystallization kinetics in terms of improved nucleation sites through three methods—interface engineering, ligand-assisted engineering, and antisolvent engineering. Notably, we review recent progress in additive strategies, vapor-assisted crystallization and temperature-mediated crystallization in the field of perovskites and elaborate on the regulation of perovskite crystallization kinetics from the perspective of delayed crystal growth. Moving beyond conventional approaches, this review provides a critical examination of often-overlooked factors in crystallization control. We highlight the decisive role of interfacial acidity in preventing deprotonation during nucleation and establish the acid dissociation constant (pK_a) of additives as a key descriptor for the stability of blue perovskite precursors. Particular emphasis is placed on solution supersaturation dynamics, the nature of additive-induced intermediate phases, and the influence of environmental conditions. Finally, we summarize the current challenges in this field and offer a forward-looking perspective, providing theoretical support for achieving high-quality perovskite displays.

Yang Shen

Yang Shen received his MSc (2020) and PhD (2023) degrees in Materials Science from Soochow University of China. Then, he joined FUNSOM at Soochow University as a research lecturer. His research interests lie in flexible electronics, optical manipulation by nanostructures, and interfacial engineering of metal-halide perovskite light-emitting diodes.

Yan-Qing Li

Yan-Qing Li received her BSc degree in physics from Zhejiang University, and her MPhil and PhD degrees in Materials Science from City University of Hong Kong. She is now a professor at the School of Physics and Electronics Science, East China Normal University. Her main research interests lie in organic and inorganic/organic hybrid materials and devices with a focus on flexible electronics, involving the synthesis, characterization, and device integration of metal and semiconductor nanostructures and thin films for a range of device applications including light-emitting diodes and solar cells.

Jian-Xin Tang

Jian-Xin Tang received his BSc degree in physics from Zhejiang University, and PhD degree in Physics and Materials Science from City University of Hong Kong. In 2008, he was appointed professor at FUNSOM, Soochow University. In 2021, he was appointed professor at the Macao Institute of Materials Science and Engineering (MIMSE), Macau University of Science and Technology. His research areas/interests span device physics and surface science of organic/perovskite light-emitting diodes and photovoltaic cells.

2 Perovskite nucleation and crystal growth

2.1 Nucleation

The formation of perovskite films exhibiting high crystallinity and pinhole-free morphology is governed primarily by solution supersaturation, nucleation, and crystal growth processes.[29] Nucleation, a critical precursor to solution phase transition, is predominantly driven by precursor solution supersaturation. The nucleation rate influences the density and distribution of nuclei. In classical nucleation theory, the nucleation process can be described by the total Gibbs free energy (ΔG) (Fig. 1a),[29] which consists of surface free energy (ΔG_S) and bulk free energy (ΔG_V), as shown in eqn (1):

$$\Delta G(r) = \Delta G_S + \Delta G_V = 4\pi r^2\gamma + \frac{4}{3}\pi r^3 \Delta G_V \quad (1)$$

The surface free energy represents the energy between the surface and the nucleus, primarily determined by the nucleus radius (r) and the surface free energy per unit area (γ). The volume free energy is the free energy per unit volume of the crystal, determined by the difference in free energy between the crystal and the monomers in the solution, where k_B is the Boltzmann constant, S is the supersaturation ratio of the solution, and T is the system's temperature in Kelvin, as expressed in eqn (2):

$$\Delta G_V = -\frac{k_B T \ln S}{V} \quad (2)$$

The formation of nuclei in solution strongly depends on the critical radius (r^*). Nuclei with radii smaller than r^* dissolve back into the solution, while larger nuclei with radii exceeding r^* are thermodynamically stable and will continue to grow. Therefore, the nucleation rate is determined by supersaturation, temperature, and surface free energy.[29] A reduction in surface free energy decreases the critical energy barrier for nucleation, thereby enhancing the nucleation rate. A high nucleation rate leads to more nuclei, resulting in the formation of a larger number of smaller crystals, which is beneficial for further crystal growth. To form dense perovskite films with good coverage, achieving a high nucleation rate before crystal growth is crucial. Nucleation regulation is an important means to optimize nucleation rates, including interface engineering, ligand-assisted engineering, and antisolvent engineering.[28,30–32] The fundamental principle of these methods is to suppress crystal growth while enabling rapid nucleation, which will be discussed and summarized in section 3.

2.2 Crystal growth

The growth mechanism of perovskite crystals can be explained by the LaMer model and Ostwald ripening model. Fig. 1b provides a schematic overview of the LaMer model,[29] outlining its characteristic three stages that describe the progression from monomer formation to colloidal sol formation in perovskite precursor solutions. Stage 1 is the pre-nucleation phase, where monomers rapidly accumulate in solution to reach the saturation concentration C_S. Due to the existence of an energy barrier, nucleation cannot occur at the saturation

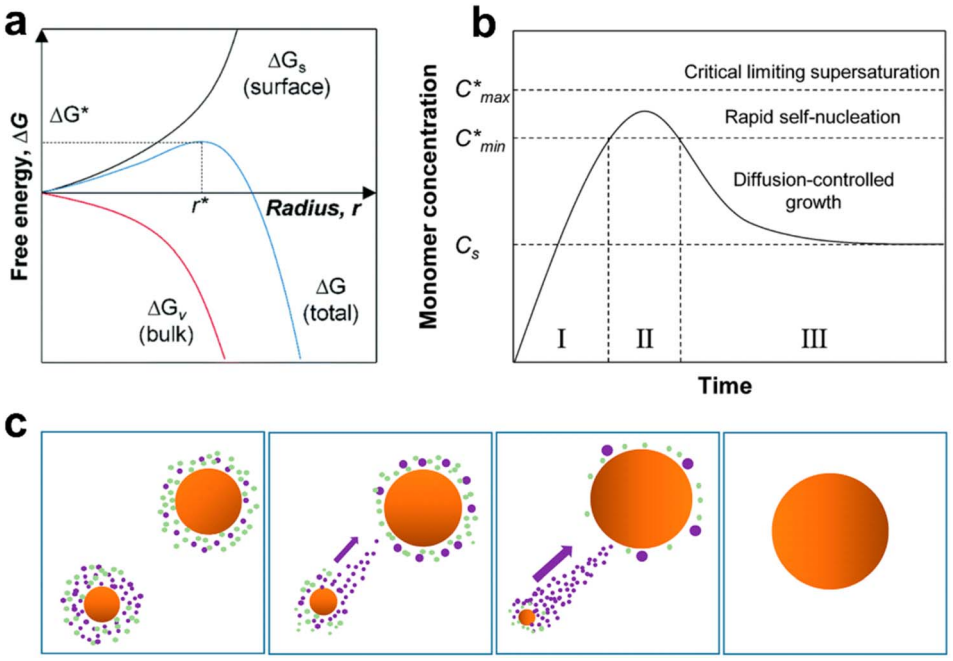

Fig. 1 (a) Schematic diagram of the classical free energy diagram for homogeneous nucleation as a function of particle radius. (b) LaMer diagram for monodispersed particle formation. Reproduced with permission from ref. 29. Copyright 2019, Royal Society of Chemistry. (c) Schematic of the Ostwald ripening model to describe the dynamic coarsening process of perovskite grains. Reproduced with permission from ref. 33. Copyright 2018, American Chemical Society.

concentration. Only when solvent evaporation continues and monomer concentration reaches the critical level C_{min}, where the Gibbs free energy exceeds the critical barrier, does the process enter Stage 2 and nucleation begins. Once nuclei form, subsequent crystal growth immediately proceeds. As nucleation solutes are continuously consumed, the nucleation process terminates when solution concentration falls below C_{min}. In Stage 3, crystals continue to grow until the monomer concentration decreases below C_S.

The Ostwald ripening model serves as another framework for explaining crystal growth (Fig. 1c).[33] According to the Gibbs–Thomson relation, smaller particles possess higher surface energy and tend to dissolve. Consequently, concentration gradients form between particles of varying sizes. These gradients, governed by Fick's first law of diffusion, drive dissolved components from smaller particles toward larger ones.[34,35] As this process continues, smaller particles gradually dissolve while larger particles grow further.[33] The Ostwald ripening mechanism has been invoked to elucidate perovskite grain growth through coalescence, where the system evolves toward minimizing its total surface energy.

3 Strategies for regulating crystallization kinetics of PeLEDs

3.1 Optimization of the nucleation sites

The uncontrollable nucleation process in solution-processed metal halide perovskites leads to random nucleation sites and excessive grain boundary formation during thin-film growth. This results in grain heterogeneity, poor film morphology with pinhole formation, increased defect-state density, reduced photoluminescence quantum yield (PLQY), and ultimately low external quantum efficiency (EQE) in PeLEDs. This section provides a comprehensive analysis of recent advancements in optimizing nucleation strategies for PeLEDs, with particular emphasis on interface engineering for substrate modulation, ligand-assisted engineering for precursor stabilization, and antisolvent engineering for optimized solvent extraction. Additionally, we discuss the current development status of these approaches and their implications for high-performance PeLEDs.

3.1.1 Interface engineering. For LED applications, suitable charge transport layers (CTLs) are crucial for device performance and stability. CTLs should possess appropriate energy levels to enable efficient charge injection/transport while blocking opposite charges. Moreover, the CTL beneath the perovskite layer is particularly critical, as it significantly influences the crystal growth of the perovskite layer and its interfacial defects.[36] According to classical nucleation theory, the key to modulating nucleation kinetics lies in reducing the surface free energy. By introducing molecules at the interface that can form strong ionic bonds or hydrogen bonds with perovskite components (*e.g.*, Pb^{2+} and halide ions), low-energy-barrier heterogeneous nucleation sites can be constructed. This strategy not only significantly enhances the nucleation driving force by lowering the interfacial free energy, making high-density nucleation thermodynamically more favorable, but also optimizes interfacial wettability to create kinetically favorable conditions for the subsequent directional growth of crystals. To increase the wettability of the substrate, Song *et al.* employed conjugated polyelectrolytes containing different counterions (TMA^+, TEA^+, and TBA^+) as hole transport layers. They found that bulky TBA^+ improved interfacial wettability through non-covalent adsorption, promoting uniform nucleation and reducing film trap density from 5.8×10^{17} cm^{-3} to 2.6×10^{17} cm^{-3}, emphasizing a critical role of larger counterions in crystallization kinetics.[37] Furthermore, the strong ionic bonding between alkali metal ions and halide ions can effectively reduce the surface free energy between perovskite nuclei and the substrate. This leads to an increased nucleation density and promotes the formation of dense, small-grained perovskite films. Based on this theory, Shen *et al.* introduced K_2SO_4 into PEDOT:PSS, leveraging the strong interaction between K^+ and halide ions to form heterogeneous nucleation sites, boosting the EQE of deep-blue PeLEDs (469 nm) to 4.14%.[38] Inspired by this, Yu *et al.* further adopted an interfacial modulation strategy using zwitterionic potassium sulfonate (PS) additives. Nuclear magnetic resonance (NMR) spectroscopy verified the hydrogen bonding interaction between PS and halide ions. Because of the formation of hydrogen bonds, the K^+ in PS acted as nucleation sites, guiding uniform perovskite crystallization and suppressing halide vacancy formation, significantly improving the performance of pure-blue PeLEDs.[14] However, the aforementioned studies fail to provide a mechanistic understanding of the underlying chemical principles. Therefore, Cao *et al.* detailed the chemical reactions involved in interface engineering and perovskites. They introduce a rapid *in situ* interface reaction at the buried interface between the perovskite layer and the underlying PEDOT:PSS film. This engineered interface reaction represents a novel method for preparing high-quality deep-blue $CsPb(Br/Cl)_3$ films. By incorporating weakly acidic lithium salicylate (SAL) as a reaction initiator into the perovskite precursor, a proton exchange is triggered between PEDOT:PSS and SAL, resulting in the formation of a multifunctional PSS–Li interfacial layer. This layer modulates perovskite nucleation and growth, producing compact, uniform, and small-grained deep-blue perovskite films with reduced trap densities and enhanced quantum confinement. The resulting spectrally stable deep-blue PeLEDs achieve a record EQE of 12.3% at 468 nm (Fig. 2a).[39] The pH at the buried interface critically governs perovskite film growth by modulating precursor protonation states and reactivity. Specifically, an alkaline surface deprotonates organic ammonium ions into volatile neutral amines. This irreversible consumption of organic species disrupts the stoichiometric balance, thereby driving the formation of non-photoactive yellow-phase perovskite crystals. To address this issue, Jin *et al.* selected an organic ammonium cation with weak acidity [guanidinium (Gua^+)] and paired it with an interfacial layer of tunable basicity achieved through the conversion of $Zn(OH)_2$ to amorphous ZnO (a-ZnO) to fabricate high quality $CsPbI_3$. Fig. 2b illustrates a schematic of the switchable interfacial deprotonation reaction based on ZnO with different levels of basicity and ammonium cations with

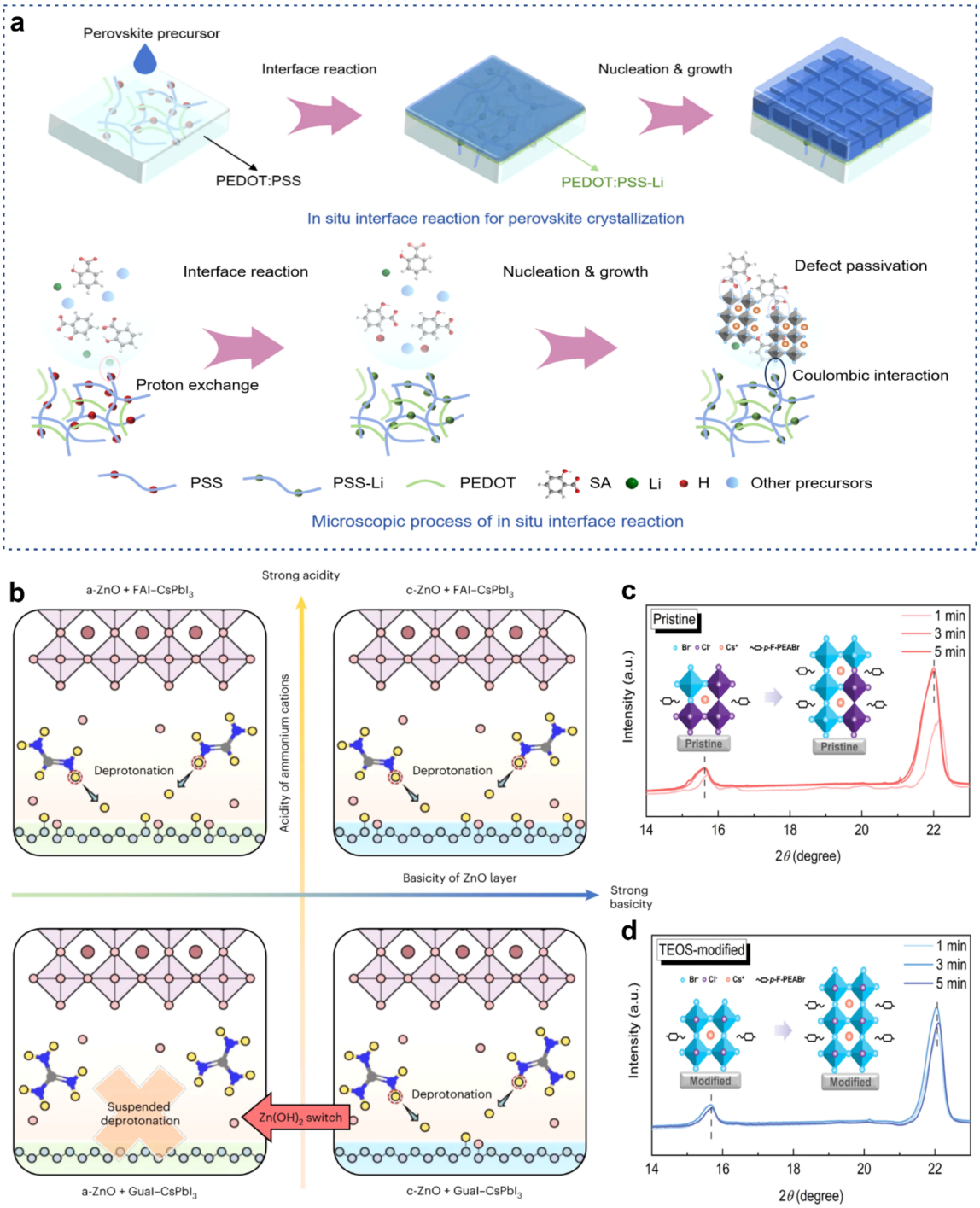

Fig. 2 (a) *In situ* interface reactions of perovskite crystals after the introduction of SAL. Reproduced with permission from ref. 39. Copyright 2025, Wiley-VCH. (b) Schematic of switchable interfacial deprotonation reactions based on ZnO with varying basicity and ammonium cations with different acidities. Reproduced with permission from ref. 40. Copyright 2024, Springer Nature. (c) Schematic diagram of XRD for the crystallization process of pristine blue perovskite films. (d) Schematic diagram of XRD for the crystallization process of TEOS-modified blue perovskite films. Reproduced with permission from ref. 46. Copyright 2024, Wiley-VCH.

different acidities. The key to switching the deprotonation reaction lies in the transition from the fourth quadrant to the third quadrant, facilitated by the annealing of initially basic $Zn(OH)_2$ into a-ZnO film. This process effectively suppresses the formation of the undesired yellow-phase $CsPbI_3$ perovskite. As a result, the resulting $CsPbI_3$-based PeLEDs achieve an exceptionally high radiance of approximately 1980 W s^{-1} m^{-2}.[40] Therefore, future research should focus on precisely tuning the pH of the buried interface and conducting in-depth theoretical analysis at the chemical level, rather than relying on simple

material substitution which leads to merely incremental performance improvement. Additionally, employing ions such as Cs^+ and GA^+ as pre-nucleation seeds to regulate the nucleation and crystallization of quasi-2D perovskites can enhance charge transport, optimize band alignment, and induce phase redistribution. This reduces the formation of low-*n* phases (*e.g.*, $n = 1$, 2) while promoting high-*n* phase growth, thereby minimizing non-radiative recombination defects and demonstrating superior device performance in red, green and blue PeLEDs.[41–43] Introducing molecules at the interface that interact with the perovskite to reduce surface free energy *via* ionic bonding represents a critical strategy for controlling nucleation kinetics, which is essential for growing high-crystallinity, pinhole-free perovskite films. Small-molecule additives modifying the hole transport layer can provide abundant nucleation sites before perovskite nucleation, facilitating the formation of dense perovskite films.[44] Tang *et al.* implemented an interfacial nucleation seeding (INS) strategy by incorporating ethanolamine (ETA) into PEDOT:PSS. The amino ($-NH_2$) and hydroxyl (–OH) groups in ETA formed hydrogen bonds with halide ions, providing heterogeneous nucleation sites and suppressing grain growth. This approach reduced the grain size of $CsPbBr_{3-x}Cl_x$ perovskite films from 26.5 nm to 20.2 nm, significantly lowering trap density and enhancing exciton radiative recombination efficiency. Combined with internal light-extraction nanostructures, the EQE of blue PeLEDs (486 nm) increased from 6.3% to 16.8%, while device stability improved markedly.[45] Furthermore, constructing an *in situ* growth network at the buried interface improves substrate wettability, which is conducive to achieving highly crystalline perovskite films. The influence of the buried interface on perovskite crystallization has been elucidated through *in situ* characterization techniques, providing theoretical guidance for understanding mixed-halide crystallization kinetics. Wang *et al.* introduced a multifunctional tetraethyl orthosilicate (TEOS) network as a grain growth substrate to regulate perovskite crystallization kinetics, achieving a high PLQY of 75.2%. The crystallinity changes of perovskite films at different annealing times were detected by equivalent *in situ* grazing-incidence wide-angle X-ray scattering (GIWAXS). As shown in Fig. 2c and d,[46] when the annealing time was extended from 1 minute to 3 minutes, the diffraction peaks of the pristine film underwent a significant shift toward lower angles, indicating gradual expansion of the perovskite lattice over time. In this case, as crystallization began, $PbCl_2$ precursors first entered the perovskite lattice, followed by $PbBr_2$ participating in the formation of the final mixed-halide perovskite film. This phenomenon can be attributed to the poorer solubility of Cl-rich perovskite phases compared to their Br-rich counterparts. In contrast, the diffraction peaks of the modified film remained at constant angles, indicating synchronous crystallization of Cl^- and Br^- components in the perovskite lattice, thus resulting in octahedral crystals with uniform halogen distribution. Therefore, by utilizing the buried TEOS molecular network to promote grain growth and balanced crystallization of mixed-halide perovskite phases, rational regulation of perovskite crystallization can be achieved.[46]

In addition, introducing an ultrathin hydrophilic polymer between the perovskite precursor and the substrate significantly improves the interfacial energy, thereby reducing the nucleation barrier and increasing the nucleation rate. For example, You *et al.* synergistically regulated the nucleation and crystallization of $CsPbBr_3$ *via* polyvinyl pyrrolidine (PVP) modification and MA^+ doping. Specifically, PVP-modified ZnO electron transport layers enhanced substrate hydrophilicity, promoting uniform precursor spreading, reducing film pinholes, and passivating interfacial defects. Simultaneously, a small amount of MA^+ ($Cs_{0.87}MA_{0.13}PbBr_3$) optimized crystallization kinetics through molecular anchoring effects, suppressing Pb metallic defects and improving film compactness. Ultimately, the PeLEDs exhibited high brightness (91 000 cd m^{-2} at 520 nm) and a high EQE of 10.4%.[47] It should be noted that although polymer interlayers such as PVP are highly effective in improving substrate wettability and regulating perovskite crystallization, their wide-bandgap and insulating properties represent a "double-edged sword". An excessively thick PVP layer would undoubtedly introduce a high charge injection barrier between the perovskite layer and the electron transport layer (*e.g.*, ZnO), hindering the effective flow of electron carriers and consequently leading to increased device resistance and reduced efficiency. Therefore, the key to successfully applying such strategies lies in the precise control of the polymer layer thickness, making it sufficiently thin to maintain efficient tunneling effects or direct charge carrier transport while still fully leveraging its role in regulating crystallization and passivating the interface. Furthermore, modulating the solid–liquid interfacial interaction between perovskite precursors and substrates using hydrophilic carbonized polymer dots (CPDs) optimized nucleation, achieving oriented crystal alignment. Without CPDs, cation-dominated interactions led to uneven nucleation and ring-like film formation. In contrast, CPDs shifted the interaction to anion dominance, promoting uniform nucleation and dense film growth. The surface amino groups of CPDs interacted with sulfonic acid groups on the substrate, regulating ion adsorption, reducing defects, and inducing crystal alignment.[48] This approach significantly improved film uniformity and luminescence efficiency, offering a novel strategy for the efficient fabrication of large-area PeLEDs.

3.1.2 Ligand engineering. The modulation of solvent–precursor interactions to control solution supersaturation represents another approach for regulating nucleation rates. Organic ligands influence supersaturation levels by consuming precursor species. Through TA analysis, Sargent *et al.* discovered that strong van der Waals interactions between stacked bulky organic spacer cations (PEA^+) most favorably facilitate the formation of $n = 1$ 2D perovskites, resulting from colloidal precursor aggregation. This process consumes a substantial amount of organic cations in precursor solution, reduces nucleation sites, and leaves short-chain precursors (those associated with the repeat unit of 3D crystals) to nucleate phases with high *n* values. However, exciton recombination in high-*n* domains causes undesired emission redshift, while low-*n* ($n = 1$) domains may induce strong electron–phonon coupling and consequent non-radiative recombination losses.[49] Moreover,

inferior energy transfer efficiency deteriorates the optoelectronic properties of perovskites. Introducing Lewis base additives has become an effective strategy to passivate defects and retard high-*n* domain growth *via* coordination interactions. Ren *et al.* incorporated bifunctional cations containing both amino and carboxyl groups to weaken van der Waals forces and enhance coupling in layered quasi-2D perovskites.[50] By quantifying Lewis base coordination affinity, Zhou *et al.* found that moderate interaction restricts high-*n* phase nucleation while promoting low-*n* phase growth, leading to a more concentrated phase distribution and improved energy transfer.[51] Various zwitterions with different Pb^{2+} coordination affinities serve dual roles as passivators and co-spacer organic layers in quasi-2D perovskites, disrupting colloidal precursor aggregation and shortening quantum well distances, achieving an EQE of 15.6% at 490 nm.[51] Furthermore, additives with different acid dissociation constants show great potential in regulating phase distribution. Hu *et al.* employed benzenesulfonic acid (BSA) and ammonium benzenesulfonate (ABS) with similar structures but distinct pK_a values to influence colloidal precursor aggregation.[52] High-pK_a ABS molecules reduced organic ligand adsorption energy through hydrogen bonding, yielding concentrated phase distribution with an EQE of 18.8% in sky blue PeLEDs.[52] Wu *et al.* also investigated the influence of multifunctional biopharmaceutical molecules [such as ambroxol hydrochloride (AMB), with multifunctional groups (*e.g.*, –OH and $-NH_2$) as a multifunctional perovskite crystallization regulator] on the distribution of perovskite ligands. AMB hinders the adsorption of the spacer molecule PEA onto the perovskite octahedra and improves the purity of the phase distribution (Fig. 3a).[53] This strategy promotes the formation of well-aligned layered phases and facilitates efficient exciton transfer, yielding spectrally stable sky-blue PeLEDs with a high EQE of 22.42%.[53] Beyond these methods, Choy *et al.* proposed incorporating quasi-2D perovskite solution with 2D perovskite and excess ammonium salt to synthesize novel quasi-2D perovskites. These materials exhibit phase redistribution through low-*n* phase suppression for efficient energy transfer and defect passivation, reducing trap density by over 60% to diminish nonradiative recombination. The monodispersity of layered 2D perovskites depends on spatially uniform organic cation distribution in precursor solutions.[54,55] To obtain a single-phase distribution, Jiang *et al.* developed a ligand structure (utilizing MBA, an analog of PEA) to control the synthesis of monodisperse ultra-small quantum dots. The head group of the ligand (the side with higher electrostatic potential) provides steric hindrance that inhibits the formation of layered perovskites. The tail (the side with lower electrostatic potential) was modified *via* halide substitution to enhance surface binding affinity, confining the resulting crystal grains to sizes within the quantum confinement regime (Fig. 3b and c).[18] As a result, they reported blue PeLEDs with an EQE of 18% at 480 nm and 10% at 465 nm.[20]

Co-interlayer engineering represents another strategy for van der Waals interaction modulation. Minor structural changes in interlayer materials can significantly impact final performance, as charge tunneling between sites in quasi-2D perovskites strongly depends on wavefunction overlap between adjacent localized states.[56–58] Additionally, microscopic morphology formation and trap distribution are precisely affected by ligand material properties. Su *et al.* developed efficient quasi-2D perovskites using phenylbutylammonium bromide (PBABr) and propylammonium bromide (PABr) as ligands. Adjusting co-interlayer component ratios improved film morphology and phase distribution, significantly enhancing PLQY to 89%.[59] To suppress $n = 1$ phase nucleation, shorter ligands were introduced to weaken van der Waals interactions, enhancing high-*n* phase purity and dispersity. The resulting films exhibited single emission peaks and color-stable blue emission (477 nm) with 88% PLQY, maintaining wavelength stability under 325 nm (7 W cm^{-2}) irradiation for 1 hour.[49] Furthermore, long-chain ligands with large steric hindrance positively influence phase distribution. Fang *et al.* demonstrated that amantadine hydrobromide (AMAN) effectively disrupts PEABr aggregation through steric hindrance, isolating PEABr molecules to prevent low-*n* phase formation ($n \leq 3$) and promote concentrated phase distribution. *In situ* photoluminescence studies revealed that AMAN delays nucleation and crystallization by adsorbing on perovskite surfaces and impeding epitaxial growth, enabling champion devices to achieve an EQE of 30.84% (Fig. 3d and e).[60]

3.1.3 Antisolvent engineering. Antisolvent engineering represents another effective approach for achieving rapid nucleation of perovskite films. The fundamental principle lies in the introduction of an antisolvent that is miscible with the initial solvent but cannot dissolve the perovskite precursors. This rapidly reduces the solubility in the system, accelerating the attainment of a supersaturated state and driving nucleation. As described by the LaMer model, a burst in nucleation density occurs only when the monomer concentration exceeds the critical nucleation supersaturation. Highly volatile antisolvents can rapidly reach this threshold, leading to instantaneous, high-density nucleation, thereby facilitating the formation of pinhole-free perovskite films. Lee *et al.* reported uniform surface coverage and reduced grain size by using chloroform to wash out the polar solvents [dimethylformamide or dimethyl sulfoxide (DMSO)]. Chloroform was chosen as the solvent for accelerated nucleation because a highly volatile nonpolar solvent is suitable to reduce the size and increase the uniformity of $MAPbBr_3$ grains by reducing solvent evaporation time. In contrast, micrometer-sized $MAPbBr_3$ cuboids were scattered on the hole transport layer without antisolvent engineering. They were only interconnected with a few other cuboids, so a large amount of space remained uncovered. This high surface roughness and the formation of pinholes in perovskite films result in the formation of a poor interface with the electron transport layer and electrical shunt paths, thus severely limiting EQE in PeLEDs.[61] Yu *et al.* employed chlorobenzene as an antisolvent to rapidly remove excess DMSO solvent and reduce perovskite solubility in the precursor solution, quickly achieving supersaturation and realizing fully surface-covered perovskite films. Building on this, incorporating organic small molecules into the antisolvent transforms it into a carrier for *in situ* delivery of passivators. These passivators are uniformly transported to the surfaces of nuclei and grain boundaries,

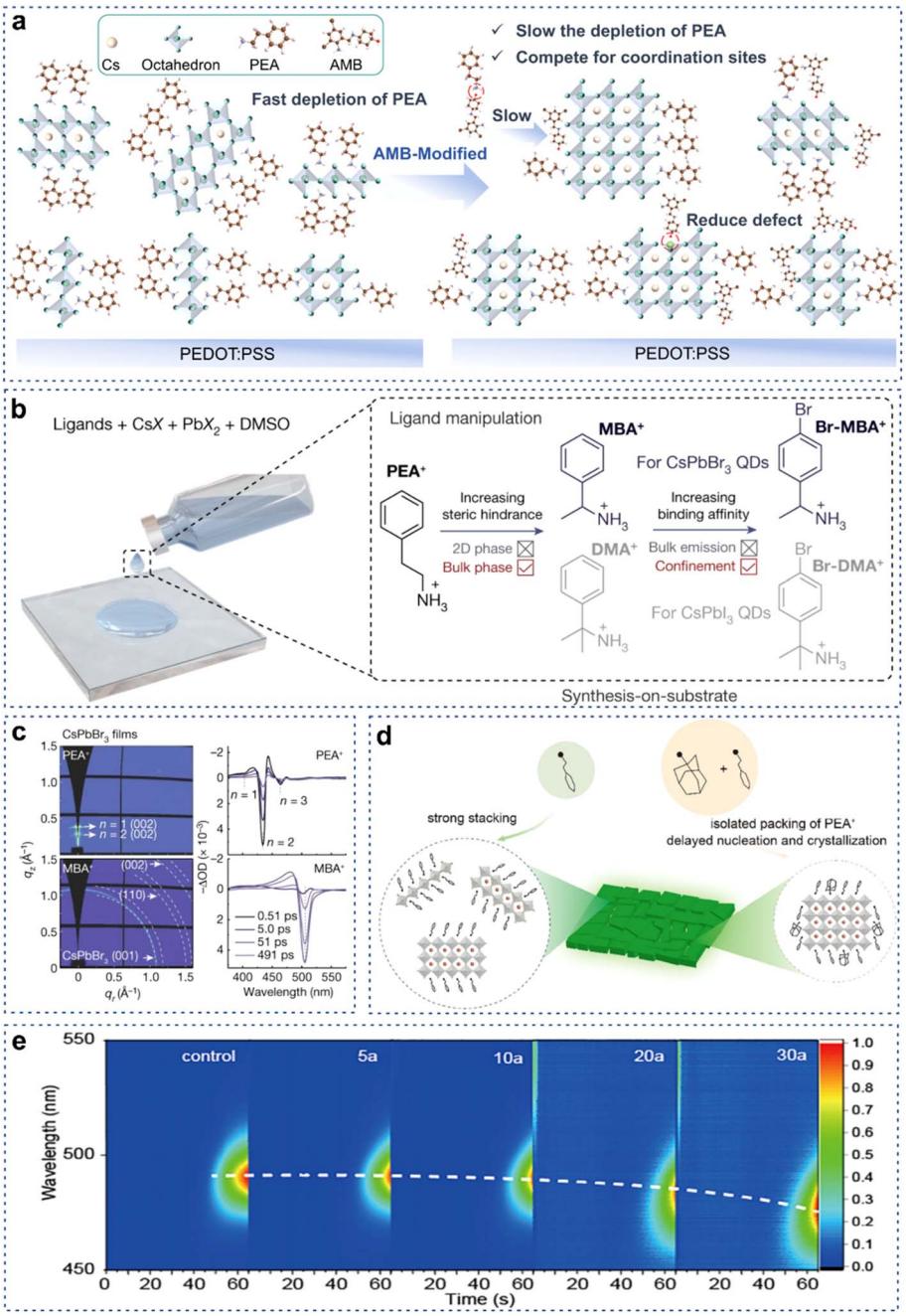

Fig. 3 (a) Schematic illustration of the impacts of AMB on the PEA dynamics and phase distribution during the crystallization of quasi-2D perovskite films. Reproduced with permission from ref. 53. Copyright 2025, American Chemical Society. (b) Molecular structures and properties of different PEA-like ligands. (c) GIWAXS patterns of $CsPbBr_3$ and transient absorption spectra of $CsPbBr_3$ with PEA and MBA as ligands. Reproduced with permission from ref. 18. Copyright 2022, Springer Nature. (d) Schematic diagram of AMAN regulating the nucleation and crystallization processes. (e) *In situ* PL measurements of perovskite films. Reproduced with permission from ref. 60. Copyright 2025, Wiley-VCH.

enabling *in situ* passivation of the perovskite. This process effectively modulates the photoluminescence quantum yield (PLQY) of the film.[62] You *et al.* utilized a small amount of ethyl acetate (EA) mixed with ETPTA as an antisolvent, which was dripped onto the spinning quasi-film. This treatment induced instantaneous nucleation and immediately froze the constituents into the perovskite crystals. The ETPTA layer could conformably cover the surface of the perovskite film with intimate contact and permeate into the perovskite layer along the grain boundaries during the washing process, resulting in a threefold increase in the T_{50} operational time of the devices compared to the control sample.[63] Furthermore, Ma *et al.* reported that the surface morphology and crystal structure of perovskite films strongly depend on antisolvent treatment, leading to improved grain orientation and a smooth surface. They successfully obtained PEABr–$CsPbI_3$ epitaxial films with

larger and more oriented β-$CsPbI_xBr_{3-x}$ grains (Fig. 4a).[64] This approach achieved reduced EQE roll-off, maintaining a high efficiency of 17.2% at luminance exceeding 1000 cd m^{-2}.[64] In contrast, antisolvents with lower volatility facilitate a gradual approach to critical supersaturation, opening a controllable window for delayed nucleation. Kim *et al.* employed that the use of toluene mixed with weakly coordinating isopropanol to control precursor supersaturation and assist perovskite crystallization, achieving a grain size of 39 nm and much stronger photoluminescence intensity. The strategy employs the differential solubility of CsBr in the mixed antisolvent to modulate the nucleation kinetics of perovskite, as shown in Fig. 4b.[65] The corresponding $CsPbBr_3$ PeLEDs exhibited approximately twice the maximum current efficiency (a CE_{max} of 94.64 cd A^{-1}) and an EQE_{max} of 22.93% compared to control devices. Additionally, Xiao *et al.* utilized *in situ* UV-Visible spectroscopy to investigate the formation kinetics of perovskite nanocrystals (PNCs) under antisolvent conditions. Precursors begin to nucleate after the antisolvent dripping and the nucleation is completed rapidly within 1.5 s, as observed by tracking the evolution of the absorbance. This work provides insights into the crystallization process of perovskite nanocrystals under the influence of antisolvent.[66] However, conventional antisolvent dripping methods face fundamental limitations in controlling crystallization kinetics, particularly manifesting as instantaneous nucleation and severe spatial inhomogeneity in scaled-up perovskite films. Wang *et al.* developed a microdroplet-phase antisolvent deposition technique that establishes a controlled crystallization environment through delayed nucleation kinetics *via* mild antisolvent interaction and uniform microdroplet diffusion across extended substrates (Fig. 4c).[67] A remarkable EQE of 23.21% is also realized when the active area expands to 6.25 cm^2 in green PeLEDs. In summary, the rate at which antisolvent engineering induces supersaturation directly dictates the nucleation density and final grain size. Rapid solvent extraction tends to form uniform and dense perovskite films with fine grains, whereas a slower extraction process facilitates the formation of large-grained perovskite crystals with high uniformity. Therefore, the selection of antisolvents in the future should be tailored to the specific morphological requirements of the target device.

3.2 Delayed crystallization

Crystal growth is an important stage in the preparation of high-quality perovskite films. The rapid growth process leads to disadvantages such as grain aggregation, high defect density, and poor orientation, which severely restrict the light emission performance. In this section, the impact of delayed crystallization on PeLEDs is comprehensively examined. The delayed

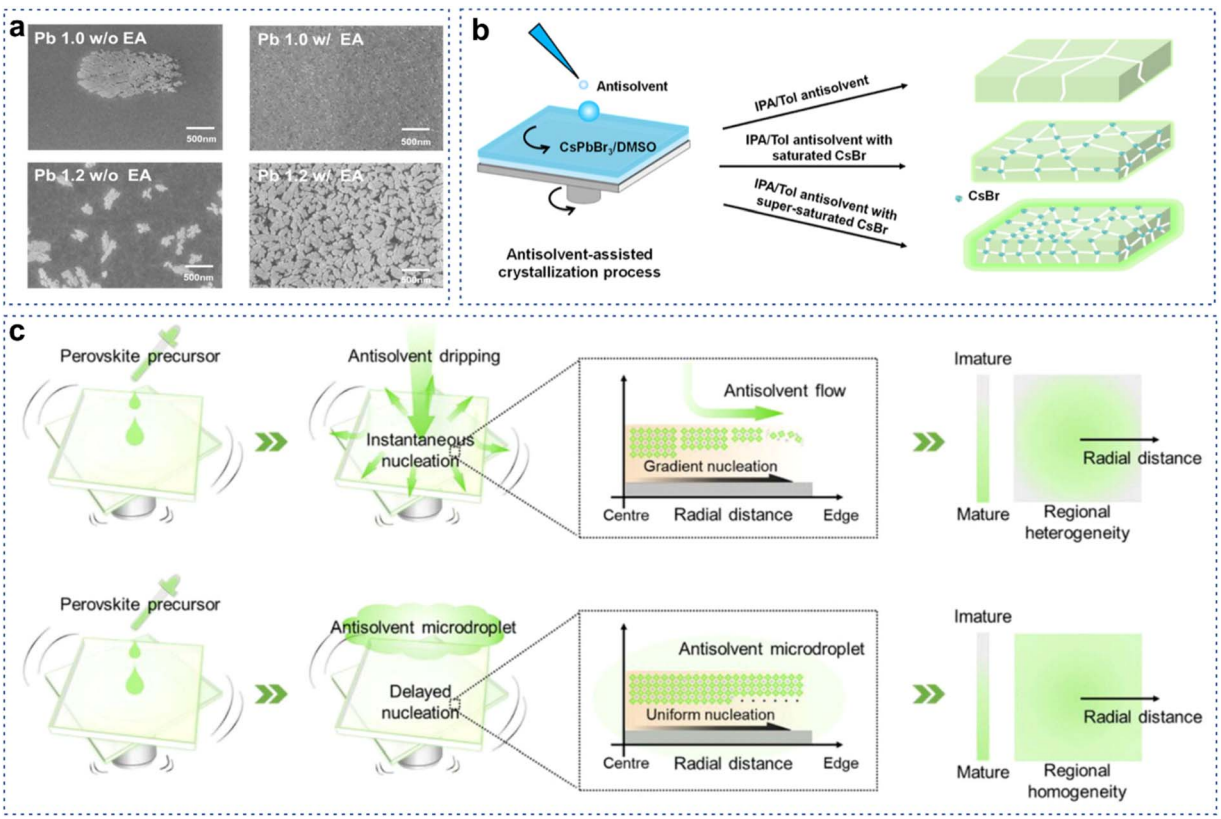

Fig. 4 (a) SEM images of Pb1.0 and Pb1.2 films without and with EA treatment, respectively. Reproduced with permission from ref. 64. Copyright 2022, Wiley-VCH. (b) Schematic illustration of antisolvent-assisted crystallization. Reproduced with permission from ref. 65. Copyright 2024, American Chemical Society. (c) Schematic diagram illustrating the superiority of the antisolvent microdroplet strategy over the traditional antisolvent dripping procedure. Reproduced with permission from ref. 67. Copyright 2025, Wiley-VCH.

crystallization process is systematically summarized, focusing on three key aspects: the role of additives, steam-assisted crystallization and temperature control. This analysis provides a detailed understanding of how these factors influence the crystallization kinetics and, consequently, the performance of PeLEDs. By elucidating the mechanisms underlying delayed crystallization, this section aims to offer valuable insights for optimizing the fabrication of high-quality perovskite films and advancing the development of efficient and stable PeLEDs.

3.2.1 Additive engineering. The introduction of suitable additives into perovskite precursors to retard crystal growth is crucial for achieving high-quality perovskite films, including Lewis acid–base additives and organic small molecules. The delayed crystallization kinetics establishes a vital processing window, which is essential for enabling effective defect passivation by additives and promoting a uniform halide distribution in mixed-halide systems. The functional groups of additives (–NH_2, –OH, –COOH, –P═O, *etc.*) can passivate undercoordinated Pb^{2+} and halide anions by forming chemical bonds, suppressing non-radiative recombination loss and stabilizing the grain boundaries. By forming stable coordination intermediates with Pb^{2+}, the explosive crystallization is modulated into a slowed and controlled crystal growth process. Kuang *et al.* employed 5-amino valeric acid (5-AVA) as a crystallization agent and demonstrated through *in situ* X-ray diffraction (XRD), UV-Visible spectroscopy, and photoluminescence analysis that the strong coordination ability of 5-AVA with Pb^{2+} ions promotes direct nucleation of the perovskite phase while following a "fast nucleation, slow growth" mechanism to retard crystal growth (Fig. 5a).[68] This well-controlled crystallization kinetics results in enhanced crystallinity, reduced defect density, and a narrower cascade phase distribution in quasi-2D perovskite.

Ultimately, these improvements enabled pure-red PeLEDs to achieve higher EQE (increasing from 15.68% to 21.23%) and extended operational lifetime (from 242 to 506 minutes).[68] Utilizing the chelation effect of functional groups with Pb can achieve delayed crystal growth. Gao *et al.* compared two highly efficient chelating molecules with their respective monofunctionalized counterparts, finding that chelation-enhanced Pb-additive binding affinity enables the formation of chemically stable intermediates that effectively suppress perovskite nucleation and delay crystal growth. This delayed crystallization process yielded highly emissive perovskite films and efficient near-infrared (NIR) PeLEDs with EQE exceeding 20% (Fig. 5b).[69] Furthermore, Xiao *et al.* combined surface ligands with the chelating molecules to control the growth of colloidal PNCs. We explored the combination of 4F-PEA with δ-aminovaleric acid hydrobromide, that is, δ-AVA HBr, reasoning that the carboxyl group can modify the reaction rate, while the ammonium group—compared to the amine group of δ-AVA^-—may more effectively interact with PNC surfaces by occupying FA^+ vacancies. More encouragingly, δ-AVA HBr temporally separates crystal growth from nucleation: crystal growth occurs after 10 s of thermal annealing and slowly saturates within 7 s. Due to the improved crystallization, the δ-AVA HBr film displays a blue-shifted PL peak compared to the control (524 nm *vs.* 531 nm) as well as the absence of 2D perovskites and $PbBr_2$ phases in XRD patterns. The average film PLQY was thus improved to 64%. More importantly, this strategy resulted in modified PNCs with an average size of 6.8 ± 1.6 nm and uniform film morphology.[66] To further enhance the crystal size of perovskite, Peng *et al.* introduced sacrificial additives—hypophosphorous acid and ammonium chloride—into the precursor to induce the nucleation and crystallization of $CsPbBr_3$. Following high-temperature annealing, the resulting material exhibited an absence of thermal quenching and formed single-crystalline grains exceeding several hundred nanometers in size, with minimal trap density (Fig. 5c).[12]

In addition to retarding crystal growth by forming complexes with precursors, additives can also preemptively occupy lattice sites to impede crystal growth. Due to the different growth rates of bromine-based and chlorine-based perovskites in the mixed halide blue perovskite, the distribution of halogens becomes heterogeneous. To address the ion migration issue faced by mixed halides, Zhang *et al.* found that increasing local lattice distortion (LLD) can raise the ion migration energy barrier. They verified that methylene diammonium (MDA^{2+})-substituted perovskites exhibit suppressed halide migration under continuous illumination and an electric field, particularly at high chloride alloying rates, *e.g.*, $CsPb(Br_{0.6}Cl_{0.4})_3$ perovskite. This method effectively suppressed defect generation.[70] Furthermore, Wang *et al.* utilized multidentate bonding to interact with the perovskite lattice simultaneously at both the A-site and X-site, significantly enhancing the operational stability of deep-blue PeLEDs, leading to a half-lifetime of 144 min at a constant current density of 0.45 mA cm^{-2}.[19] However, the inherent multifunctionality of single-additive systems remains underexplored.

Furthermore, polymer additives tend to segregate at the grain boundaries during the later stages of perovskite crystallization and growth. On the one hand, they can fill the voids at the grain boundaries; on the other hand, they can chemically link adjacent grains, consequently enhancing the mechanical and electrical stability of the boundaries. Crowns, with their highly selective complexation capability for specific cations, are commonly employed polymer additives in PeLEDs. Ning *et al.* developed a supramolecular dynamic coordination-induced segmented crystallization of perovskite emitters, where crown ether and sodium trifluoroacetate coordinated with A-site and B-site ions. *In situ* characterization showed that coordination suppressed nucleation of perovskite crystals and growth of low-dimensional structures, exhibiting excellent luminescence quantum yield and efficient carrier injection (Fig. 6a).[71] Building on this work, Jiang *et al.* further elucidated the mechanism of crown ethers as supramolecular enhancers for perovskite device performance. They discovered strong interactions between crown ethers and precursors, with *in situ* PL proving that crown ether addition significantly delayed perovskite crystallization, providing insights into supramolecular–perovskite interaction modes (Fig. 6b).[23]

B-site alloying represents another approach to retard crystallization and improve film quality. Huang *et al.* applied alloying to blue perovskites using Rb/Cs alloying to retard crystal growth, suppress current leakage, and enhance optical

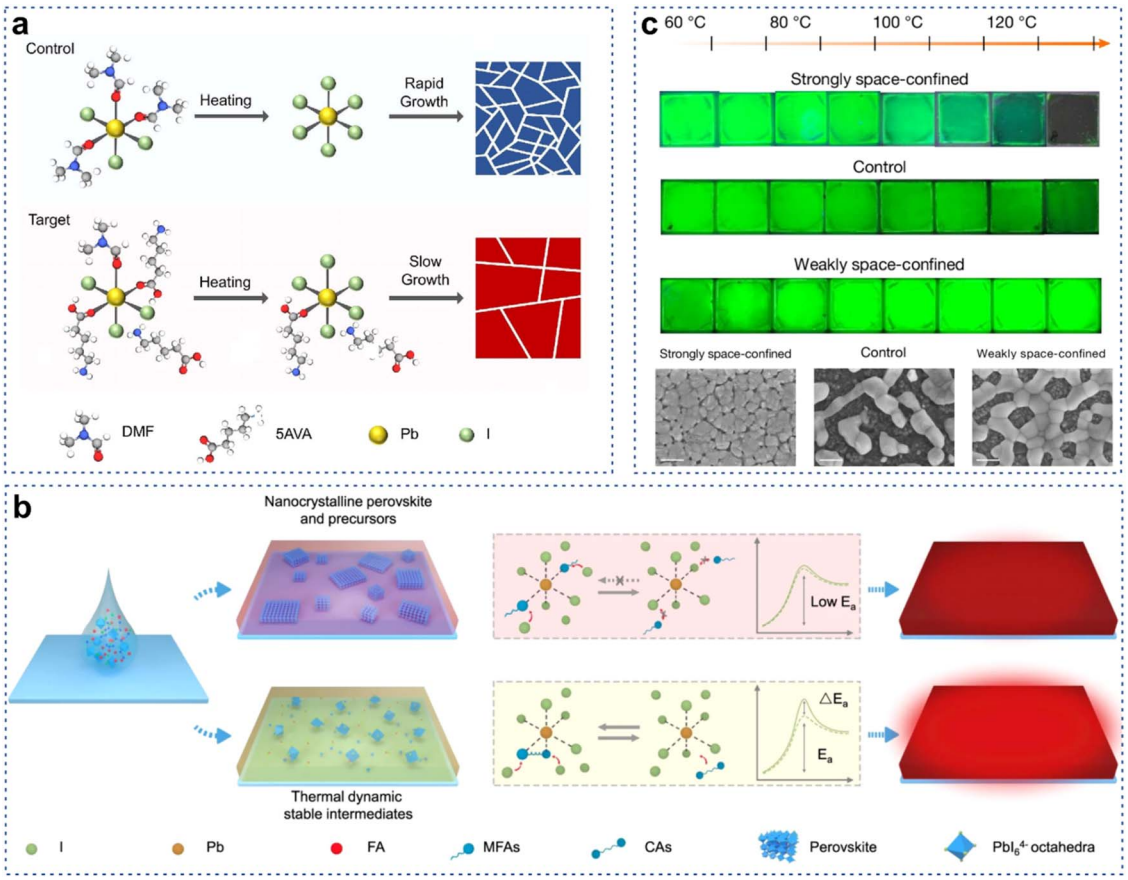

Fig. 5 (a) Schematic illustration of perovskite crystallization mechanisms. Reproduced with permission from ref. 68. Copyright 2025, Elsevier. (b) Schematic illustration of the perovskite crystallization process with different lead-additive binding affinities. Reproduced with permission from ref. 69. Copyright 2021, Springer Nature. (c) Photoluminescence images of perovskite films with different annealing temperatures (60–130 °C, in 10 °C intervals) for 10 min and top-view SEM images of the strongly space-confined, control and weakly space-confined perovskite films. Reproduced with permission from ref. 12. Copyright 2025, Springer Nature.

coupling, achieving ultrahigh brightness of 14 000 cd m^{-2} at 475 nm.[72] Chen *et al.* demonstrated through scanning electron microscopy (SEM) and XRD analysis of films annealed for different durations that Sr-doped perovskites undergo slower, stepwise crystallization, achieving films with high PLQE of 80% and an EQE of 23.3% at 487 nm (Fig. 6c).[73] Additionally, Zhao *et al.* achieved record radiance in NIR PeLEDs through A-site cation alloying, where excess FAI triggered compact wide-bandgap intermediate phases that transformed into isolated, highly crystalline grains during annealing, suppressing non-radiative losses. However, when further increasing x from 90 to 120, the crystallinity of the perovskite films started to drop, indicating that under this condition the high concentration of FAI has started to impede the crystal growth of perovskites as shown in Fig. 6d. It should be noted that the positive effects of excess FAI in enhancing the crystal growth of the perovskite film are verified for different precursor concentrations.[74] In summary, a fundamental role of additive engineering is to create a slow and controllable crystallization environment for the system. The resulting retarded crystal growth permits lattice self-repair and orderly assembly of the perovskite during annealing, which serves as a prerequisite for achieving high-quality crystals and uniform films. Ideally, an additive molecule should contain multiple functional sites and diverse mechanisms, enabling its molecular structure to simultaneously retard crystallization, passivate defects, stabilize grain boundaries, and/or suppress ion migration. The synergistic effects among these functionalities are key to achieving performance breakthroughs.

3.2.2 Vapor-assisted crystallization. Vapor-assisted crystallization (VAC) has emerged as an effective approach for controlling perovskite crystal growth kinetics and improving film quality. This technique involves exposing perovskite precursor films to solvent or reactant vapor during thermal annealing, enabling a more controlled crystallization process compared to conventional solution methods. In earlier work in this field, Gao *et al.* demonstrated spectrally stable blue PeLEDs (490–451 nm) through vapor-phase processing, which suppressed local compositional inhomogeneity and ion migration. They conducted SEM measurements to track the grain growth and morphological evolution of the films during the VAC treatment. The first stage happens within the first minute of vapour treatment, showing crystal growth from initially formed small grains into large ones (Ostwald ripening), accompanied

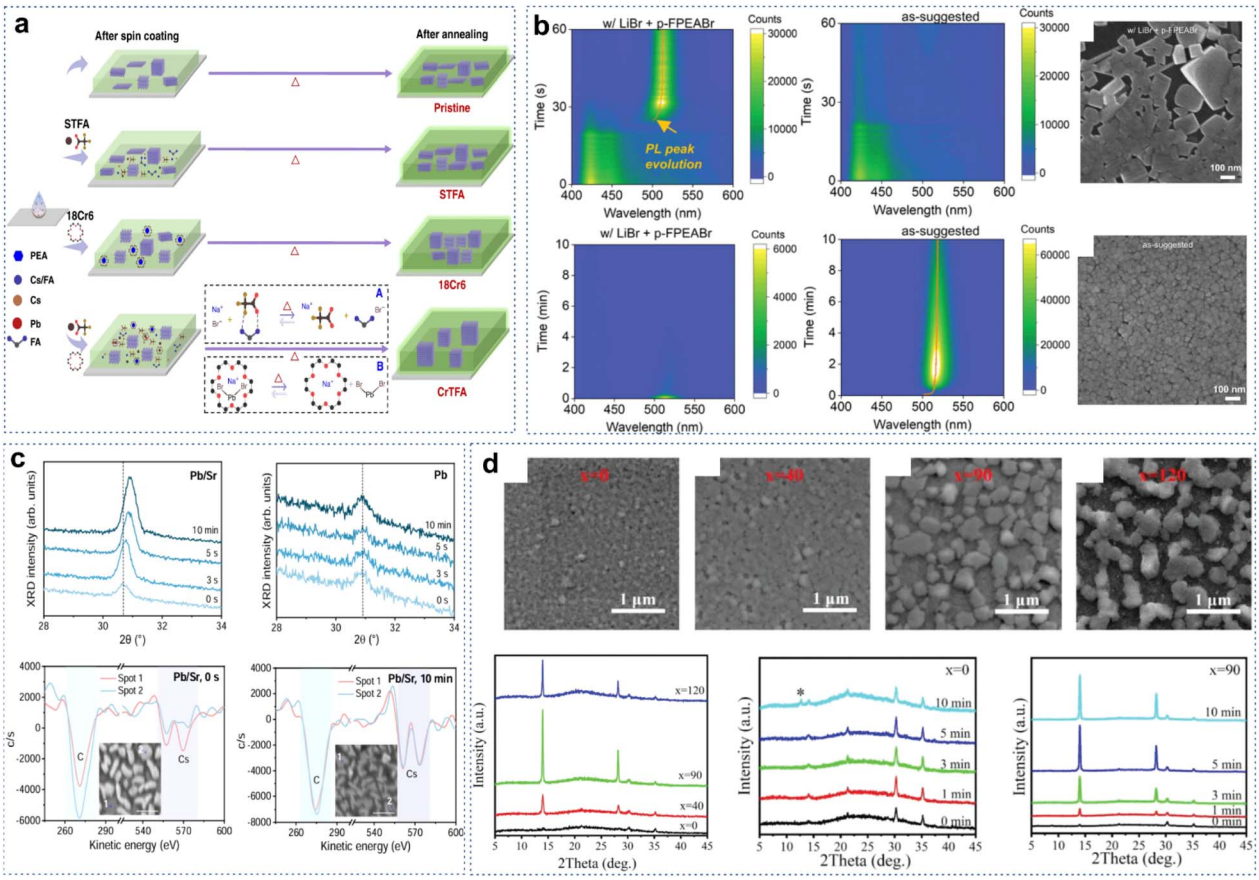

Fig. 6 (a) Crystal growth kinetics of films without and with STFA, 18Cr6, and CrTFA. Reproduced with permission from ref. 71. Copyright 2023, Springer Nature. (b) *In situ* PL measurement and SEM for films w/LiBr + *p*-FPEABr and w/LiBr + *p*-FPEABr + Crown. Reproduced with permission from ref. 23. Copyright 2024, Wiley-VCH. (c) Characterization of perovskite films with different annealing times. Reproduced with permission from ref. 73. Copyright 2025, Springer Nature. (d) SEM images and XRD patterns of perovskite films fabricated with 0, 40, 90, and 120 excess FAI; XRD patterns of perovskite films with different amounts of excess FAI during annealing. Reproduced with permission from ref. 74. Copyright 2020, Wiley-VCH.

by the morphological evolution from dense films into a discontinuous network. The second stage happens during the prolonged duration of treatment. The wet films preserved by DMF vapour can be regarded as a sol system, with the solvent as the dispersing medium and perovskites as the dispersed phases. The ripening process occurs because large grains are more energetically favoured than smaller grains, leading to reduced grain boundaries and hence fewer defects (Fig. 7a).[75] Notably, their 3D perovskite-based blue and deep-blue LEDs exhibited high EQEs of 11.0% and 5.5% with emission peaks at 477 nm and 467 nm, respectively. Feng *et al.* recently reported a mixed-vapor strategy using volatile carbon disulfide (CS_2) and a precursor solvent atmosphere (SA) for optimizing *in situ* crystallization of red perovskite films. They investigated the interaction between CS_2 molecules and red perovskites. As a small-size Lewis base, CS_2 molecules are continuously adsorbed onto perovskite crystals to passivate the under-coordinated Pb atoms and block halide ion migration. More importantly, the presence of SA/CS_2 mixed vapor facilitates gradual crystal growth that is dominated by thermodynamics, thus avoiding phase disproportionation governed by kinetic control (Fig. 7b).[76] Consequently, the mixed vapor treated perovskite films exhibit greatly inhibited energy loss due to the reduced trap states and accelerated exciton transfer. This sophisticated vapor design achieved record EQE values across the deep-red to pure-red spectral ranges along with exceptional operational stability.[76] The processing technique also enabled controlled crystal growth in both blue and green spectral regions. As illustrated, Li *et al.* employed *in situ* GIWAXS to monitor crystallization dynamics during solvent-free annealing and solvent vapor-assisted annealing (SVAA), providing a detailed investigation of perovskite crystallization kinetics. Scanning electron microscopy images further revealed that perovskite growth followed Ostwald ripening at higher solvent concentrations. By varying the solvent vapor concentration during annealing, perovskite grain sizes could be tuned from 200 nm to several micrometers. This work provides a comprehensive elucidation of solvent atmosphere effects on perovskite structure, offering valuable guidance for future development of high-quality perovskite films (Fig. 7c).[77]

3.2.3 Temperature-controlled crystallization. The intrinsically low formation energy and soft ionic lattice structure of

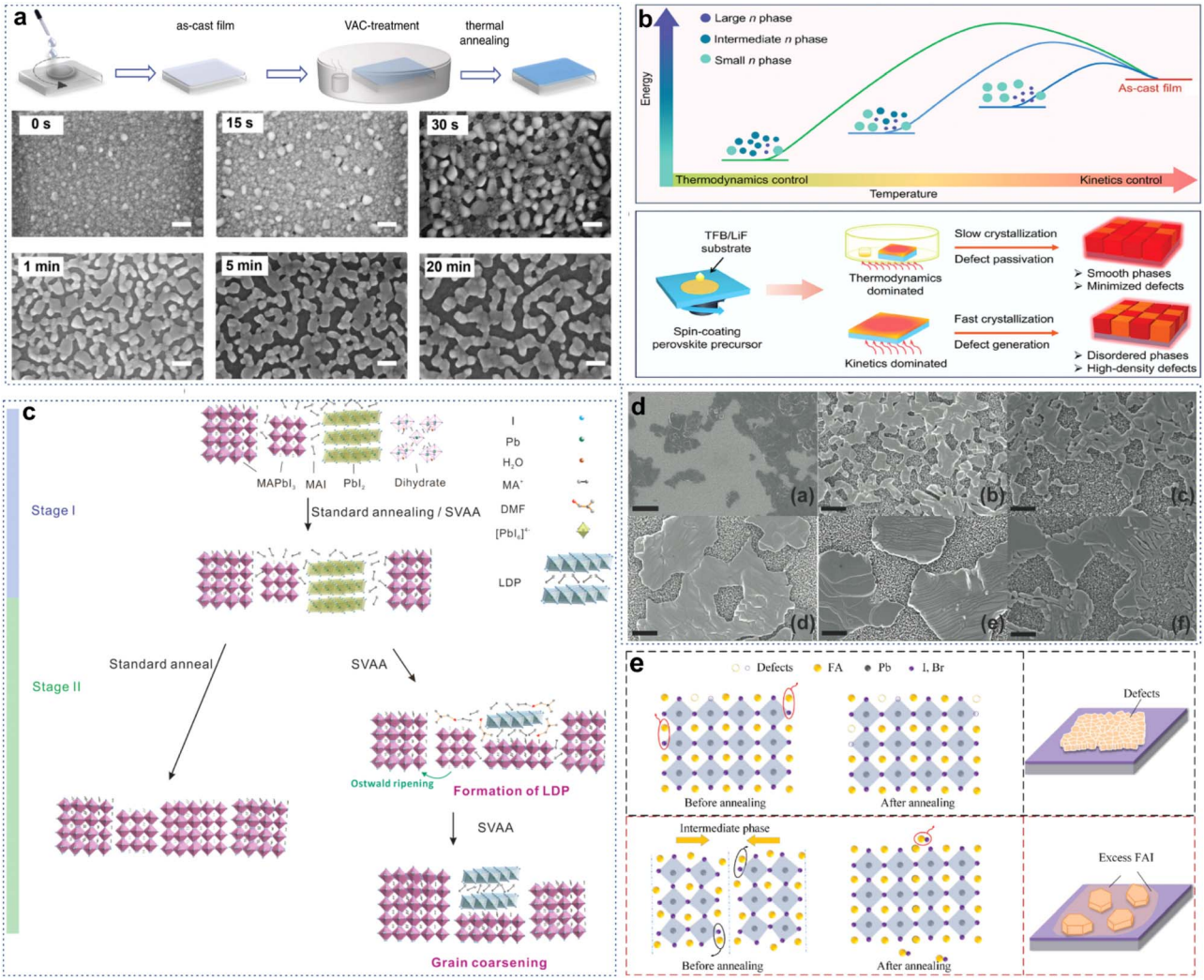

Fig. 7 (a) An illustration of the VAC-treatment; top-view SEM images showing the growth/coalescence of grains during the VAC treatment. Reproduced with permission from ref. 75. Copyright 2021, Springer Nature. (b) Perovskite crystallization control strategy. Reproduced with permission from ref. 76. Copyright 2024 Wiley-VCH. (c) Schematic of $MAPbI_3$ formation during standard annealing and SVAA. Reproduced with permission from ref. 77. Copyright 2021, American Chemical Society. (d) SEM images of $mTiO_2$ films with deposited perovskite solution heat treated at (a) 60 °C, (b) 80 °C, (c) 100 °C, (d) 120 °C, (e) 150 °C, and (f) 175 °C. Reproduced with permission from ref. 78. Copyright 2014, Wiley-VCH. (e) Scheme for the proposed crystallization process of perovskite films without excess FAI ($x = 0$) and with 90 excess FAI ($x = 90$). Reproduced with permission from ref. 74. Copyright 2020 Wiley-VCH.

perovskite materials endow them with rapid nucleation and growth kinetics. As a critical parameter, temperature enables precise regulation of these crystallization processes. Dualeh *et al.* systematically investigated the impact of annealing temperature on perovskite films, revealing that elevated temperatures (>100 °C) frequently induce PbI_2 secondary phase formation. Their work established that moderate annealing temperatures (60–80 °C) optimally retard crystal growth to produce high-quality films with suppressed defects (Fig. 7d).[78] In systems with excess FAI, the annealing process plays a critical role in determining the morphology of the resulting perovskite film. Upon annealing the excess FAI molecules gradually drive the merging of the layered structures to form a 3D perovskite lattice with preferred orientation. After the perovskite framework formation, part of the excess FAI may aggregate around the crystal grains, thereby passivating defects on the grain boundaries. The excess FAI may also fill the gaps between the isolated grains. The presence of these FAI molecules may help reduce the leakage current during PeLED operation (Fig. 7e).[74] Advancing this understanding, Song *et al.* demonstrated temperature-controlled growth of highly ordered perovskite single crystals through optimized thermal protocols. The resulting crystals exhibited minimized trap densities and maximized bimolecular radiative recombination rates, enabling PeLEDs with exceptional color purity (FWHM = 19.5 nm) and EQE exceeding 12%.[79] Additionally, Yao *et al.* utilized low-temperature annealing to minimize lattice strain in $CsPbI_{3-x}Br_x$ films caused by inhomogeneous halide distribution, resulting in planar defect-free $CsPbI_{3-x}Br_x$ films with improved radiative recombination, a narrowed emission band, and

enhanced spectral stability.[80] Wang *et al.* revealed that the enhanced EQE at low temperatures stems from improved PLQY of the perovskite emission layer, which is attributed to accelerated radiative recombination rates. Spectroscopic studies and computational simulations demonstrate that the phase transition of $FAPbI_3$ plays a pivotal role in enhancing exciton binding energy, with the strengthened excitonic effect subsequently boosting recombination rates. These findings suggest promising potential for PeLEDs in spacecraft and space communication applications.[81]

4 Summary and outlook

In this review, we systematically discuss the fundamental principles of perovskite nucleation and crystal growth, and provide a comprehensive overview of recent advances based on two key strategies: optimized nucleation sites and delayed crystal growth. The central theme of this review lies in modulating the crystallization dynamics of perovskites—particularly through precise control over nucleation and growth processes—to optimize thin-film quality and ultimately enhance the optoelectronic performance of PeLEDs. We focus on various optimized strategies, including interface engineering, ligand-assisted engineering, antisolvent engineering, additive engineering, vapor-assisted crystallization, and temperature-mediated crystallization, with the aim of elucidating the relationship between crystallization mechanisms and device performance. However, PeLEDs still face bottlenecks in achieving commercial-scale production. The following discussion will address these challenges.

4.1 High efficiency blue PeLEDs for full-color displays

To achieve full-color displays, it is essential to develop efficient red, green, and blue PeLEDs. However, blue PeLEDs still exhibit significantly inferior performance compared to their red and green counterparts, which represents a major bottleneck for the commercialization of perovskite-based displays.[15,82–84] The performance of blue PeLEDs is primarily limited by three factors: first, blue perovskite materials largely rely on either high Cl/Br ratios or large organic cations to modulate the bandgap (the former leads to poor spectral stability, and the latter hinders charge transport);[85,86] second, it is difficult to achieve precise regulation of the phase distribution of 2D perovskites, thereby hindering the attainment of high color purity and high luminescence efficiency;[2,14,87] third, the blue perovskite emission layer possess a relatively deep hole injection barrier, resulting in imbalanced charge injection.[14,18,85] Precise design of spacer molecules, such as aromatic amines or sterically hindered amines, enables fine control over the quantum well width and phase purity, thereby simultaneously achieving high color purity and high luminescence efficiency.[88] Consequently, the development of novel functionalized organic spacer molecules has become a major research focus. In addition, exploring new perovskite crystal structures with intrinsically wide bandgaps—coupled with size control *via* nanocrystal morphology and surface chemistry modulation—offers a promising route to stable blue emission. Innovative strategies such as *in situ* halide ion exchange or the ingenious design of interfacial reactions utilizing the specific properties of additives and the hole transport layer to enhance quantum confinement effects represent powerful approaches for achieving tunable blue emission.[39] Furthermore, the design of new hole/electron transport materials enables more balanced carrier injection, reducing Joule heating and non-radiative recombination. The introduction of interlayers with better energy-level alignment and ion-blocking functionality can effectively suppress detrimental interdiffusion and reactions between the perovskite layer and electrodes, significantly enhancing the operational stability of the devices. Despite the formidable challenges, research on blue PeLEDs is advancing at an unprecedented pace. Future progress will undoubtedly be a highly interdisciplinary endeavour, requiring synergistic innovation across materials chemistry, device physics, optical engineering, and manufacturing processes.

4.2 Lead-free tin-based PeLEDs

Current research on PeLEDs predominantly focuses on Pb-based perovskites; however, their inherent toxicity significantly hinders large-scale industrial application. Among alternative materials, tin-based perovskites have emerged as one of the most promising candidates due to their comparable optoelectronic properties. Nevertheless, several critical challenges remain: Uncontrolled crystallization kinetics during film formation frequently induces structurally defective morphologies characterized by high-density pinholes and intergranular boundaries. Such defective morphology adversely affects charge transport, promotes photoluminescence quenching, and compromises device stability. Furthermore, the inherent susceptibility to oxidative conversion from Sn^{2+} to Sn^{4+} establishes a thermodynamically favored oxidation pathway, resulting in substantial defect densities within the lattice framework. To address the rapid crystallization of Sn-based perovskites, Lee *et al.* employed the strongly coordinating Lewis base DMPU to suppress Sn^{2+} oxidation in precursor solutions while promoting uniform and highly crystalline film growth. DMPU-based PeLEDs showed substantially improved brightness and stability.[89] Xie *et al.* further introduced the antioxidant additive reduced L-glutathione (GSH) to modulate crystallization rates, where hydrogen bonding and coordination between GSH and PEA_2SnI_4 effectively reduced crystallization rates, suppressed Sn^{2+} oxidation, and minimized defect formation. The optimized pure-red PeLEDs achieved a record EQE of 9.32% in PEA_2SnI_4-based devices.[90] These additive-based strategies demonstrate significant potential for improving the performance of tin-based PeLEDs, thereby paving the way for the industrialization of Pb-free perovskite optoelectronics. Therefore, future research should prioritize the development of multifunctional additives and the exploration of potent reducing agents and encapsulation strategies to prevent oxidation of tin-based perovskites during both fabrication and device operation.

4.3 Operational stability of PeLEDs

There exists an inherent trade-off between the operational stability and the rapidly enhanced EQE of PeLEDs, which consequently restricts their practical application in display technologies. This limitation primarily stems from several intrinsic loss mechanisms: charge trapping induced by defects within the perovskite emissive layer, Auger recombination at high charge carrier densities, and charge quenching due to imbalanced charge injection.[91–93] Collectively, these factors lead to significant EQE roll-off at high current densities, thereby impairing operational stability. Maintaining high EQE at high current densities is critical to mitigating Joule heating effects and thus improving operational stability.[20] Recent studies have demonstrated promising strategies to address these challenges. Xiao *et al.* reported an alternative strategy to overcome Auger recombination based on weakly space-confined all-inorganic perovskite. Owing to suppressed Auger recombination, the EQE remained above 20% even at high current densities approaching 1000 mA cm^{-2}. Furthermore, the operational stability was significantly enhanced, with the weakly spatially confined PeLEDs exhibiting an extended T_{50} of 185 600 hours at an initial luminance of 100 cd m^{-2} at room temperature.[12] In addition, the breakage of the $[PbX_6]^{4-}$ framework severely deteriorated carrier mobility, leading to the severe Joule heating, low efficiency and poor device stability. To address this issue, Yao *et al.* introduced strongly bonded molecules into the octahedral framework, enabling the realization of bright and efficient pure-red PeLEDs. These devices exhibit an EQE_{max} of 24.2% and low efficiency roll-off, with a T_{50} of 127 hours at 100 cd m^{-2}.[20] Furthermore, EQE role-off under high current density operation is also attributed to hole leakage resulting from unmatched device architecture design. Therefore, modulation of crystal size, efficient defect passivation, incorporation of strongly coordinating molecules into the octahedral framework to enhance lattice stability, and rational design of charge transport layers to mitigate hole leakage are essential strategies for improving device performance.[7,21,36,94–96] These approaches exhibit considerable potential for improving the operational durability of PeLEDs. Therefore, future research should prioritize the suppression of EQE roll-off, underscoring the urgent need for innovations in passivation materials and the development of optimized charge transport layer configurations.

4.4 Large-area PeLEDs for displays

At present, the vast majority of fabricated PeLEDs remain limited to small-scale devices. For large-area PeLEDs, intrinsic film inhomogeneity leads to unsatisfactory performance with significant pixel-to-pixel variations. The core challenge lies in the rapidly declining controllability of the crystallization process as the device area increases, making it difficult to ensure uniform thin-film morphology. Furthermore, the coffee-ring effect—wherein solvent evaporates more rapidly at the periphery, causing solute migration and accumulation at the edges—results in the formation of non-uniform ring-shaped films that are thicker at the boundaries and thinner in the center. Therefore, it is imperative to develop cost-effective and scalable fabrication processes suitable for practical display production. Promising approaches for large-area PeLED displays include blade coating and inkjet printing. For instance, Xiao *et al.* employed blade-coating technology coupled with solvent kinetic modulation to achieve uniform large-area full-color devices. White PeLEDs fabricated *via* blade coating exhibited a respectable EQE of 10.6% on an active area of 0.04 cm^2, while maintaining uniform emission over areas as large as 28 cm^2.[97–99] Inkjet printing offers unique advantages such as digital control of droplet positioning, precise patterning of complex structures, high material utilization, compatibility with multilayer integration, and roll-to-roll process compatibility, making it highly suitable for high-throughput production.[100–102] Several studies have reported flexible devices and large-area modules with efficiencies exceeding 20%, building upon earlier advancements in perovskite solar cells as a reference for PeLED applications.[30] However, techniques such as blade coating and inkjet printing require precise matching with the viscosity, surface tension, and drying kinetics of perovskite precursors, thus posing challenges in terms of reproducibility and process control. Current research focuses on optimizing solvent formulations, additive engineering, controlling antisolvent dripping rates, and substrate preheating to regulate solvent evaporation—all aimed at achieving uniform and high-quality large-area displays.[103] Thermal evaporation has also been proposed as a viable route for the scalable manufacturing of PeLED displays, owing to its excellent uniformity and compatibility with existing OLED production lines. Nevertheless, this method faces limitations such as high equipment costs, poorly controlled crystal orientation, and film inhomogeneity. Crucially, there is still a lack of fundamental studies to provide meaningful guidance for optimizing the performance of evaporated perovskite-based light-emitting devices.[104–106] Consequently, substantial future research efforts are required in the field of large-area PeLEDs to address these challenges and pave the way toward their commercial adoption.

4.5 Toward the commercialization of PeLEDs: accelerating material and process optimization *via* machine learning

In the fabrication process of conventional PeLEDs, the screening of process parameters and the design of material systems significantly affect device performance. Precisely regulating process parameters (such as precursor components and concentration, spin coating parameters, solvent atmosphere, annealing temperature and time) is crucial to achieving high crystallization quality and uniformity of perovskite films. Conventional approaches typically involve extensive trial-and-error experimentation to identify optimal film-forming conditions, a process that is often time-consuming, costly in terms of research and development, and inherently inefficient. Given the aforementioned context, robotic learning has emerged as a promising methodology to tackle this challenge, leveraging its data-driven precision in prediction, the high-throughput experimentation enabled by automated systems, and the global optimization afforded by intelligent algorithms. In recent years, a growing number of researchers worldwide have

undertaken extensive investigations in this rapidly advancing field. Among them, Xu *et al.* innovatively integrated an automated nanocrystal synthesis module, a real-time spectral characterization module, and a machine learning decision-making module to construct a closed-loop experimental system of "synthesis–characterization–optimization".[107] This system establishes a reproducible technical paradigm for the efficient development of high-performance metal halide perovskite nanocrystals. The deep integration of robotic learning into perovskite materials research transcends the mere juxtaposition of isolated technological components. Looking forward, interdisciplinary collaboration across algorithms, automated platforms, and materials science will enable precise customization of molecular architectures tailored to specific performance metrics, while facilitating dynamic parameter adjustment based on real-time feedback during device fabrication. Such capabilities are critical to enhancing the reproducibility and performance uniformity of perovskite-based devices. Ultimately, establishing structure–interaction relationships through machine learning is poised to not only facilitate transformative advances in PeLED performance but also accelerate the widespread commercialization of devices that combine high luminance efficiency, extended operational stability, and scalable, low-cost manufacturing over large areas.

Author contributions

Conceptualization, Y. L., Y. S., and J. T.; writing – original draft, L. C. and Y. Z.; writing – review & editing, L. C., Y. Z., Y. L., Y. S. and J. T.; supervision, Y. L., Y. S., and J. T.

Conflicts of interest

The authors declare no competing interests.

Data availability

Data for this review article are available from the references.

Acknowledgements

The authors acknowledge financial support from the National Natural Science Foundation of China (No. 62320106004, 62274117, and 62405208), the Science and Technology Development Fund (FDCT), Macao SAR (No. 0018/2022/A1), the Natural Science Foundation of Jiangsu Province (No. BK20240777), the Collaborative Innovation Center of Suzhou Nano Science & Technology, and the Fundamental Research Funds for the Central Universities.

Notes and references

1 Z.-K. Tan, R. S. Moghaddam, M. L. Lai, P. Docampo, R. Higler, F. Deschler, M. Price, A. Sadhanala, L. M. Pazos, D. Credgington, F. Hanusch, T. Bein, H. J. Snaith and R. H. Friend, *Nat. Nanotechnol.*, 2014, **9**, 687–692.
2 M. Yuan, L. N. Quan, R. Comin, G. Walters, R. Sabatini, O. Voznyy, S. Hoogland, Y. Zhao, E. M. Beauregard, P. Kanjanaboos, Z. Lu, D. H. Kim and E. H. Sargent, *Nat. Nanotechnol.*, 2016, **11**, 872–877.
3 J. Byun, H. Cho, C. Wolf, M. Jang, A. Sadhanala, R. H. Friend, H. Yang and T. W. Lee, *Adv. Mater.*, 2016, **28**, 7515–7520.
4 K. Lin, J. Xing, L. N. Quan, F. P. G. de Arquer, X. Gong, J. Lu, L. Xie, W. Zhao, D. Zhang, C. Yan, W. Li, X. Liu, Y. Lu, J. Kirman, E. H. Sargent, Q. Xiong and Z. Wei, *Nature*, 2018, **562**, 245–248.
5 Y. Cao, N. Wang, H. Tian, J. Guo, Y. Wei, H. Chen, Y. Miao, W. Zou, K. Pan, Y. He, H. Cao, Y. Ke, M. Xu, Y. Wang, M. Yang, K. Du, Z. Fu, D. Kong, D. Dai, Y. Jin, G. Li, H. Li, Q. Peng, J. Wang and W. Huang, *Nature*, 2018, **562**, 249–253.
6 B. Zhao, S. Bai, V. Kim, R. Lamboll, R. Shivanna, F. Auras, J. M. Richter, L. Yang, L. Dai, M. Alsari, X.-J. She, L. Liang, J. Zhang, S. Lilliu, P. Gao, H. J. Snaith, J. Wang, N. C. Greenham, R. H. Friend and D. Di, *Nat. Photonics*, 2018, **12**, 783–789.
7 M. Li, Y. Yang, Z. Kuang, C. Hao, S. Wang, F. Lu, Z. Liu, J. Liu, L. Zeng, Y. Cai, Y. Mao, J. Guo, H. Tian, G. Xing, Y. Cao, C. Ma, N. Wang, Q. Peng, L. Zhu, W. Huang and J. Wang, *Nature*, 2024, **630**, 631–635.
8 Y. Yu, B. F. Wang, Y. Shen, Y. T. Wang, Y. H. Zhang, Y. Y. Li, Z. H. Su, L. X. Cao, S. C. Feng, Y. H. Wu, X. Y. Gao, S. Kera, N. Ueno, J. X. Tang and Y. Q. Li, *Adv. Mater.*, 2025, 2503234.
9 H. Li, Y. Feng, M. Zhu, Y. Gao, C. Fan, Q. Cui, Q. Cai, K. Yang, H. He, X. Dai, J. Huang and Z. Ye, *Nat. Nanotechnol.*, 2024, **19**, 638–645.
10 Y. Gao, H. Li, X. Dai, X. Ying, Z. Liu, J. Qin, J. Guo, Z. Han, Y. Zhang, M. Zhu, X. Wu, Q. Cai, Y. Yang, L. Feng, X. Zhang, J. Huang, H. He, F. Gao and Z. Ye, *Nat. Electron.*, 2024, **7**, 487–496.
11 K. Zhang, Y. Shen, L.-X. Cao, Z.-H. Su, X.-M. Hu, S.-C. Feng, B.-F. Wang, F.-M. Xie, H.-Z. Li, X. Gao, Y.-Q. Li and J.-X. Tang, *Nat. Commun.*, 2024, **15**, 10621.
12 C. Peng, H. Yao, O. Ali, W. Chen, Y. Yang, Z. Huang, H. Liu, J. Li, T. Chen, Z. Li, M. Sun, H. Zhou, X. Tao, N. Wang, J. Wang and Z. Xiao, *Nature*, 2025, **643**, 96–103.
13 X. Zhou, Z. Ren, Z. Zheng, C. Luo, H. Chen, H. Peng, B. Hu and Y. Chen, *Adv. Funct. Mater.*, 2025, **35**, 2412894.
14 Y. Yu, B. F. Wang, Y. Shen, Z. H. Su, K. Zhang, H. Ren, Y. F. Zhang, X. Gao, J. X. Tang and Y. Q. Li, *Angew. Chem., Int. Ed.*, 2024, **63**, e202319730.
15 J. S. Kim, J.-M. Heo, G.-S. Park, S.-J. Woo, C. Cho, H. J. Yun, D.-H. Kim, J. Park, S.-C. Lee, S.-H. Park, E. Yoon, N. C. Greenham and T.-W. Lee, *Nature*, 2022, **611**, 688–694.
16 S.-D. Baek, W. Shao, W. Feng, Y. Tang, Y. H. Lee, J. Loy, W. B. Gunnarsson, H. Yang, Y. Zhang, M. B. Faheem, P. I. Kaswekar, H. R. Atapattu, J. Qin, A. H. Coffey, J. Y. Park, S. J. Yang, Y.-T. Yang, C. Zhu, K. Wang, K. R. Graham, F. Gao, Q. Qiao, L. J. Guo, B. P. Rand and L. Dou, *Nat. Commun.*, 2024, **15**, 10760.
17 J. Dong, B. Zhao, H. Ji, Z. Zang, L. Kong, C. Chu, D. Han, J. Wang, Y. Fu, Z.-H. Zhang, Y. Yang, L. Zhang, X. Yang and N. Wang, *Nat. Nanotechnol.*, 2025, **20**, 507–514.

18 Y. Jiang, C. Sun, J. Xu, S. Li, M. Cui, X. Fu, Y. Liu, Y. Liu, H. Wan, K. Wei, T. Zhou, W. Zhang, Y. Yang, J. Yang, C. Qin, S. Gao, J. Pan, Y. Liu, S. Hoogland, E. H. Sargent, J. Chen and M. Yuan, *Nature*, 2022, **612**, 679–684.
19 D. Chen, A. A. Sergeev, N. Zhang, L. Ke, Y. Wu, B. Tang, C. K. Tao, H. Liu, G. Zou, Z. Zhu, Y. An, Y. Li, A. Portniagin, K. A. Sergeeva, K. S. Wong, H.-L. Yip and A. L. Rogach, *Nat. Commun.*, 2025, **16**, 2367.
20 Y.-H. Song, B. Li, Z.-J. Wang, X.-L. Tai, G.-J. Ding, Z.-D. Li, H. Xu, J.-M. Hao, K.-H. Song, L.-Z. Feng, Y.-L. Hu, Y.-C. Yin, B.-S. Zhu, G. Zhang, H. Ju, G. Zheng, W. Hu, Y. Lin, F. Fan and H.-B. Yao, *Nature*, 2025, **641**, 352–357.
21 K. Wei, T. Zhou, Y. Jiang, C. Sun, Y. Liu, S. Li, S. Liu, X. Fu, C. Hu, S. Tian, Y. Yang, X. Fu, N. AlMasoud, S. M. H. Qaid, M. K. Nazeeruddin, H.-Y. Hsu, W.-D. Li, J. T. Kim, R. Long, W. Zhang, J. Chen and M. Yuan, *Nature*, 2025, **638**, 949–956.
22 S. Lee, J. Kim, H. Kim, C. Kim, S. Kim, C. Kim, H. Lee, B. Choi, C. Muthu, T. Kim, J. Lee, S. Lee, H. Ihee and J.-Y. Lee, *Sci. Adv.*, 2024, **10**, eadn8465.
23 M. Jiang, X. Zhang and F. Wang, *Adv. Mater.*, 2024, **36**, 2400565.
24 J. Li, P. Du, Q. Guo, L. Sun, Z. Shen, J. Zhu, C. Dong, L. Wang, X. Zhang, L. Li, C. Yang, J. Pan, Z. Liu, B. Xia, Z. Xiao, J. Du, B. Song, J. Luo and J. Tang, *Nat. Photonics*, 2023, **17**, 435–441.
25 S. Hu, S. Zeng, X. Deng, P. Hou, H. Du, Y. Dou, W. Xiong, J. Pan, Y. Peng, Y.-B. Cheng and Z. Ku, *ACS Nano*, 2025, **19**, 15018–15029.
26 S. A. Veldhuis, P. P. Boix, N. Yantara, M. Li, T. C. Sum, N. Mathews and S. G. Mhaisalkar, *Adv. Mater.*, 2016, **28**, 6804–6834.
27 F. Huang, M. Li, P. Siffalovic, G. Cao and J. Tian, *Energy Environ. Sci.*, 2019, **12**, 518–549.
28 S. Wang, X. Sun, J. Shi, R. Zhao, B. Zhang, S. Lu, P. Li, F. Li, L. Manna, Y. Zhang and Y. Song, *Adv. Mater.*, 2024, **36**, 2413673.
29 M. Jung, S.-G. Ji, G. Kim and S. I. Seok, *Chem. Soc. Rev.*, 2019, **48**, 2011–2038.
30 C. Liu, Y.-B. Cheng and Z. Ge, *Chem. Soc. Rev.*, 2020, **49**, 1653–1687.
31 Z. Wu, S. Sang, J. Zheng, Q. Gao, B. Huang, F. Li, K. Sun and S. Chen, *Angew. Chem., Int. Ed.*, 2024, **63**, e202319170.
32 K. Y. Jang, S. E. Chang, D. H. Kim, E. Yoon and T. W. Lee, *Adv. Mater.*, 2025, **37**, 2415648.
33 X. Cao, L. Zhi, Y. Li, F. Fang, X. Cui, L. Ci, K. Ding and J. Wei, *ACS Appl. Energy Mater.*, 2018, **1**, 868–875.
34 F. A. Hashim, R. R. Mostafa, A. G. Hussien, S. Mirjalili and K. M. Sallam, *Knowl. Based Syst.*, 2023, **260**, 110146.
35 H. Denny Kamaruddin and W. J. Koros, *J. Membr. Sci.*, 1997, **135**, 147–159.
36 F. Qin, M. Lu, P. Lu, S. Sun, X. Bai and Y. Zhang, *Small Methods*, 2023, **7**, 2300434.
37 C. H. Jang, A. K. Harit, S. Lee, S. H. Kim, J.-E. Jeong, J. H. Park, E. D. Jung, J. M. Ha, S. K. Kwak, H. Y. Woo and M. H. Song, *ACS Nano*, 2020, **14**, 13246–13255.
38 Y. Shen, K.-C. Shen, Y.-Q. Li, M. Guo, J. Wang, Y. Ye, F.-M. Xie, H. Ren, X. Gao, F. Song and J.-X. Tang, *Adv. Funct. Mater.*, 2021, **31**, 2006736.
39 L.-X. Cao, Y. Shen, K. Zhang, Z.-H. Su, S.-C. Feng, X.-M. Hu, Y.-H. Zhang, B.-F. Wang, Y.-Y. Li, X. Gao, W.-J. Wang, S. Kera, N. Ueno, Y.-Q. Li and J.-X. Tang, *Angew. Chem., Int. Ed.*, 2025, e202513617.
40 J. Zeng, X. Sun, Y. Liu, W. Jin, S. He, X. Zhu, K. Niu, G. Sun, J. Li, H. He, T. Sun, Z. Ye and Y. Jin, *Nat. Photonics*, 2024, **18**, 325–333.
41 Y. Y. Tang, Y. Shen, Y. Yu, K. Zhang, B. F. Wang, J. X. Tang and Y. Q. Li, *Small*, 2023, **20**, 2309309.
42 Z. Chu, W. Zhang, J. Jiang, Z. Qu, F. Ma, Y. Zhao, X. Chu, Y. Shen, Y. Li, Z. Yin, X. Zhang and J. You, *Nat. Electron.*, 2023, **6**, 360–369.
43 J. Dong, F. Lu, J. Wang, Y. Zhang, X. Ma, J. Zhou, D. Han, Z. Zang and N. Wang, *Chem. Eng. J.*, 2022, **429**, 132347.
44 Y. Shen, J. K. Wang, Y. Q. Li, K. C. Shen, Z. H. Su, L. Chen, M. L. Guo, X. Y. Cai, F. M. Xie, X. Y. Qian, X. Gao, I. S. Zhidkov and J. X. Tang, *Adv. Sci.*, 2021, **8**, 2102213.
45 Y. Shen, H.-Y. Wu, Y.-Q. Li, K.-C. Shen, X. Gao, F. Song and J.-X. Tang, *Adv. Funct. Mater.*, 2021, **31**, 2103870.
46 L. Wang, Z.-H. Su, Y. Shen, S.-C. Feng, F.-M. Xie, K. Zhang, K.-F. Meng, X. Gao, J.-X. Tang and Y.-Q. Li, *Adv. Funct. Mater.*, 2024, **34**, 2401297.
47 L. Zhang, X. Yang, Q. Jiang, P. Wang, Z. Yin, X. Zhang, H. Tan, Y. Yang, M. Wei, B. R. Sutherland, E. H. Sargent and J. You, *Nat. Commun.*, 2017, **8**, 15640.
48 F. Yang, Q. Zeng, W. Dong, C. Kang, Z. Qu, Y. Zhao, H. Wei, W. Zheng, X. Zhang and B. Yang, *Light: Sci. Appl.*, 2023, **12**, 119.
49 J. Xing, Y. Zhao, M. Askerka, L. N. Quan, X. Gong, W. Zhao, J. Zhao, H. Tan, G. Long, L. Gao, Z. Yang, O. Voznyy, J. Tang, Z.-H. Lu, Q. Xiong and E. H. Sargent, *Nat. Commun.*, 2018, **9**, 3541.
50 Z. Ren, J. Yu, Z. Qin, J. Wang, J. Sun, C. C. S. Chan, S. Ding, K. Wang, R. Chen, K. S. Wong, X. Lu, W. J. Yin and W. C. H. Choy, *Adv. Mater.*, 2020, **33**, 2005570.
51 S. Liu, Z. Guo, X. Wu, X. Liu, Z. Huang, L. Li, J. Zhang, H. Zhou, L.-D. Sun and C.-H. Yan, *Adv. Mater.*, 2023, **35**, 2208078.
52 X.-M. Hu, Y. Shen, S.-C. Feng, Z.-H. Su, K. Zhang, L.-X. Cao, B.-F. Wang, X. Gao, J.-X. Tang and Y.-Q. Li, *Adv. Funct. Mater.*, 2024, **34**, 2410143.
53 Y.-H. Wu, Y. Shen, B.-F. Wang, Y.-T. Wang, S.-C. Feng, Y. Yu, Y.-H. Zhang, Z. Su, X. Gao, Y. Li and J.-X. Tang, *ACS Nano*, 2025, **19**, 20970–20979.
54 Z. Ren, K. Wang, X. W. Sun and W. C. H. Choy, *Adv. Funct. Mater.*, 2021, **31**, 2100516.
55 Z. Ren, L. Li, J. Yu, R. Ma, X. Xiao, R. Chen, K. Wang, X. W. Sun, W.-J. Yin and W. C. H. Choy, *ACS Energy Lett.*, 2020, **5**, 2569–2579.
56 Y. Jin, Z. K. Wang, S. Yuan, Q. Wang, C. Qin, K. L. Wang, C. Dong, M. Li, Y. Liu and L. S. Liao, *Adv. Funct. Mater.*, 2019, **30**, 1908339.
57 J. Jiang, Z. Chu, Z. Yin, J. Li, Y. Yang, J. Chen, J. Wu, J. You and X. Zhang, *Adv. Mater.*, 2022, **34**, 2204460.

58 K. Chen, Q. Du, Q. Cao, C. Du, S. Feng, Y. Pan, Y. Liang, L. Wang, J. Chen and D. Ma, *Nano-Micro Lett.*, 2024, **17**, 77.
59 F. Meng, X. Liu, Y. Chen, X. Cai, M. Li, T. Shi, Z. Chen, D. Chen, H. L. Yip, C. Ramanan, P. W. M. Blom and S. J. Su, *Adv. Funct. Mater.*, 2020, **30**, 1910167.
60 C. Dong, G. Chen, S. Wang, Z. Yu, W. Ke and G. Fang, *Adv. Funct. Mater.*, 2025, **35**, 2502662.
61 H. Cho, S.-H. Jeong, M.-H. Park, Y.-H. Kim, C. Wolf, C.-L. Lee, J. H. Heo, A. Sadhanala, N. Myoung, S. Yoo, S. H. Im, R. H. Friend and T.-W. Lee, *Science*, 2015, **350**, 1222–1225.
62 M. Yu, T. Qin, G. Gao, K. Zu, D. Zhang, N. Chen, D. Wang, Y. Hua, H. Zhang, Y. B. Zhao and J. Zhu, *Light: Sci. Appl.*, 2025, **14**, 102.
63 Z. Chu, Q. Ye, Y. Zhao, F. Ma, Z. Yin, X. Zhang and J. You, *Adv. Mater.*, 2021, **33**, 2007169.
64 D. Zhang, L. Chao, G. Jin, Z. Xing, W. Hong, Y. Chen, L. Wang, J. Chen and D. Ma, *Adv. Funct. Mater.*, 2022, **32**, 2205707.
65 B. W. Kim and S. H. Im, *ACS Nano*, 2024, **18**, 28691–28699.
66 W. Yu, M. Wei, Z. Tang, H. Zou, L. Li, Y. Zou, S. Yang, Y. Wang, Y. Zhang, X. Li, H. Guo, C. Wu, B. Qu, Y. Gao, G. Lu, S. Wang, Z. Chen, Z. Liu, H. Zhou, B. Wei, Y. Liao, L. Zhang, Y. Li, Q. Gong, E. H. Sargent and L. Xiao, *Adv. Mater.*, 2023, **35**, 2301114.
67 Y. Xia, J.-C. Li, Z. Zhang, N. Li, Y. Wang, Y.-H. Li, K.-L. Wang, C.-H. Chen, J. Chen, L. Huang, Y.-T. Yang, G. Xing, B. Sun and Z.-K. Wang, *Adv. Mater.*, 2025, e06413.
68 Y. Kuang, Y. Xue, Z. Zhang, L. Yang, T. Bie, R. Li, W. Liang, N. Zhou and M. Shao, *Chem. Eng. J.*, 2025, **507**, 160278.
69 Y. Zou, P. Teng, W. Xu, G. Zheng, W. Lin, J. Yin, L. Kobera, S. Abbrent, X. Li, J. A. Steele, E. Solano, M. B. J. Roeffaers, J. Li, L. Cai, C. Kuang, I. G. Scheblykin, J. Brus, K. Zheng, Y. Yang, O. F. Mohammed, O. M. Bakr, T. Pullerits, S. Bai, B. Sun and F. Gao, *Nat. Commun.*, 2021, **12**, 4831.
70 L. Zhang, Y. Jiang, Y. Feng, M. Cui, S. Li, X. Fu, H.-Y. Hsu, C. Qin and M. Yuan, *Angew. Chem., Int. Ed.*, 2023, **62**, e202302184.
71 H. Wang, W. Xu, Q. Wei, S. Peng, Y. Shang, X. Jiang, D. Yu, K. Wang, R. Pu, C. Zhao, Z. Zang, H. Li, Y. Zhang, T. Pan, Z. Peng, X. Shen, S. Ling, W. Liu, F. Gao and Z. Ning, *Light: Sci. Appl.*, 2023, **12**, 62.
72 Y. Yang, S. Xu, Z. Ni, C. H. Van Brackle, L. Zhao, X. Xiao, X. Dai and J. Huang, *Adv. Mater.*, 2021, **33**, 2100783.
73 Y. Chen, R. Wang, G. Kusch, B. Xu, C. Hao, C. Xue, L. Cheng, L. Zhu, J. Wang, H. Li, R. A. Oliver, N. Wang, W. Huang and J. Wang, *Nat. Commun.*, 2025, **16**, 3254.
74 Y.-H. Jia, S. Neutzner, Y. Zhou, M. Yang, J. M. F. Tapia, N. Li, H. Yu, J. Cao, J.-P. Wang, A. Petrozza, C.-P. Wong and N. Zhao, *Adv. Funct. Mater.*, 2020, **30**, 1906875.
75 M. Karlsson, Z. Yi, S. Reichert, X. Luo, W. Lin, Z. Zhang, C. Bao, R. Zhang, S. Bai, G. Zheng, P. Teng, L. Duan, Y. Lu, K. Zheng, T. Pullerits, C. Deibel, W. Xu, R. Friend and F. Gao, *Nat. Commun.*, 2021, **12**, 361.
76 S.-C. Feng, Y. Shen, X.-M. Hu, Z.-H. Su, K. Zhang, B.-F. Wang, L.-X. Cao, F.-M. Xie, H.-Z. Li, X. Gao, J.-X. Tang and Y.-Q. Li, *Adv. Mater.*, 2024, **36**, 2410255.
77 Y. Zhong, D. Seeberger, E. M. Herzig, A. Köhler, F. Panzer, C. Li and S. Huettner, *ACS Appl. Mater. Interfaces*, 2021, **13**, 45365–45374.
78 A. Dualeh, N. Tétreault, T. Moehl, P. Gao, M. K. Nazeeruddin and M. Grätzel, *Adv. Funct. Mater.*, 2014, **24**, 3250–3258.
79 S. Lee, J. H. Park, Y. S. Nam, B. R. Lee, B. Zhao, D. Di Nuzzo, E. D. Jung, H. Jeon, J. Y. Kim, H. Y. Jeong, R. H. Friend and M. H. Song, *ACS Nano*, 2018, **12**, 3417–3423.
80 J. Cao, C. Yan, C. Luo, W. Li, X. Zeng, Z. Xu, X. Fu, Q. Wang, X. Chu, H. Huang, X. Zhao, J. Lu and W. Yang, *Adv. Opt. Mater.*, 2021, **9**, 2100300.
81 Y. He, J. Yan, L. Xu, B. Zhang, Q. Cheng, Y. Cao, J. Zhang, C. Tao, Y. Wei, K. Wen, Z. Kuang, G. M. Chow, Z. Shen, Q. Peng, W. Huang and J. Wang, *Adv. Mater.*, 2021, **33**, 2006302.
82 X. Luo, W. Xu, G. Zheng, S. Tammireddy, Q. Wei, M. Karlsson, Z. Zhang, K. Ji, S. Kahmann, C. Yin, Y. Zou, Z. Zhang, H. Chen, L. A. B. Marçal, H. Zhao, D. Ma, D. Zhang, Y. Lu, M. Li, C. Deibel, S. D. Stranks, L. Duan, J. Wallentin, W. Huang and F. Gao, *Matter*, 2024, **7**, 1054–1070.
83 S. C. Feng, Y. Shen, X. M. Hu, Z. H. Su, K. Zhang, B. F. Wang, L. X. Cao, F. M. Xie, H. Z. Li, X. Gao, J. X. Tang and Y. Q. Li, *Adv. Mater.*, 2024, **36**, 2410255.
84 M. Jiang, X. Zhang and F. Wang, *Adv. Mater.*, 2024, **36**, 2400565.
85 D. P. Nenon, K. Pressler, J. Kang, B. A. Koscher, J. H. Olshansky, W. T. Osowiecki, M. A. Koc, L.-W. Wang and A. P. Alivisatos, *J. Am. Chem. Soc.*, 2018, **140**, 17760–17772.
86 Y. Gao, Q. Cai, Y. He, D. Zhang, Q. Cao, M. Zhu, Z. Ma, B. Zhao, H. He, D. Di, Z. Ye and X. Dai, *Sci. Adv.*, 2024, **10**, eado5645.
87 S. Liu, Z. Guo, X. Wu, X. Liu, Z. Huang, L. Li, J. Zhang, H. Zhou, L. D. Sun and C. H. Yan, *Adv. Mater.*, 2022, **35**, 2208078.
88 K. Wang, Z.-Y. Lin, Z. Zhang, L. Jin, K. Ma, A. H. Coffey, H. R. Atapattu, Y. Gao, J. Y. Park, Z. Wei, B. P. Finkenauer, C. Zhu, X. Meng, S. N. Chowdhury, Z. Chen, T. Terlier, T.-H. Do, Y. Yao, K. R. Graham, A. Boltasseva, T.-F. Guo, L. Huang, H. Gao, B. M. Savoie and L. Dou, *Nat. Commun.*, 2023, **14**, 397.
89 F. Yuan, G. Folpini, T. Liu, U. Singh, A. Treglia, J. W. M. Lim, J. Klarbring, S. I. Simak, I. A. Abrikosov, T. C. Sum, A. Petrozza and F. Gao, *Nat. Photonics*, 2024, **18**, 170–176.
90 W. Bai, M. Liang, T. Xuan, T. Gong, L. Bian, H. Li and R. J. Xie, *Angew. Chem., Int. Ed.*, 2023, **62**, e202312728.
91 G. Xing, B. Wu, X. Wu, M. Li, B. Du, Q. Wei, J. Guo, E. K. L. Yeow, T. C. Sum and W. Huang, *Nat. Commun.*, 2017, **8**, 14558.
92 W. Zou, R. Li, S. Zhang, Y. Liu, N. Wang, Y. Cao, Y. Miao, M. Xu, Q. Guo, D. Di, L. Zhang, C. Yi, F. Gao, R. H. Friend, J. Wang and W. Huang, *Nat. Commun.*, 2018, **9**, 608.

93 Y. Jiang, M. Cui, S. Li, C. Sun, Y. Huang, J. Wei, L. Zhang, M. Lv, C. Qin, Y. Liu and M. Yuan, *Nat. Commun.*, 2021, **12**, 336.
94 L. Kong, Y. Sun, B. Zhao, K. Ji, J. Feng, J. Dong, Y. Wang, Z. Liu, S. Maqbool, Y. Li, Y. Yang, L. Dai, W. Lee, C. Cho, S. D. Stranks, R. H. Friend, N. Wang, N. C. Greenham and X. Yang, *Nature*, 2024, **631**, 73–79.
95 H. Qi, Y. Tong, X. Zhang, H. Wang, L. Zhang, Y. Chen, Y. Wang, J. Shang, K. Wang and H. Wang, *Adv. Mater.*, 2024, **36**, 2409319.
96 C. Bi, Z. Yao, J. Hu, X. Wang, M. Zhang, S. Tian, A. Liu, Y. Lu, N. H. de Leeuw, M. Sui and J. Tian, *ACS Energy Lett.*, 2023, **8**, 731–739.
97 S. Chu, Y. Zhang, P. Xiao, W. Chen, R. Tang, Y. Shao, T. Chen, X. Zhang, F. Liu and Z. Xiao, *Adv. Mater.*, 2022, **34**, 2108939.
98 S. Chu, W. Chen, Z. Fang, X. Xiao, Y. Liu, J. Chen, J. Huang and Z. Xiao, *Nat. Commun.*, 2021, **12**, 147.
99 G. Shi, Z. Huang, R. Qiao, W. Chen, Z. Li, Y. Li, K. Mu, T. Si and Z. Xiao, *Nat. Commun.*, 2024, **15**, 1066.
100 D. Li, J. Wang, M. Li, G. Xie, B. Guo, L. Mu, H. Li, J. Wang, H.-L. Yip and J. Peng, *Adv. Mater. Technol.*, 2020, **5**, 2000099.
101 Y. Liu, F. Li, L. Qiu, K. Yang, Q. Li, X. Zheng, H. Hu, T. Guo, C. Wu and T. W. Kim, *ACS Nano*, 2019, **13**, 2042–2049.
102 M. Zhu, Y. Duan, N. Liu, H. Li, J. Li, P. Du, Z. Tan, G. Niu, L. Gao, Y. Huang, Z. Yin and J. Tang, *Adv. Funct. Mater.*, 2019, **29**, 1903294.
103 Y. Xia, J. C. Li, Z. Zhang, N. Li, Y. Wang, Y. H. Li, K. L. Wang, C. H. Chen, J. Chen, L. Huang, Y. T. Yang, G. Xing, B. Sun and Z. K. Wang, *Adv. Mater.*, 2025, e06413.
104 D. Zhang, T. Huang and L. Duan, *Adv. Mater.*, 2020, **32**, 1902391.
105 P. Du, J. Li, L. Wang, L. Sun, X. Wang, X. Xu, L. Yang, J. Pang, W. Liang, J. Luo, Y. Ma and J. Tang, *Nat. Commun.*, 2021, **12**, 4751.
106 J. Ávila, C. Momblona, P. P. Boix, M. Sessolo and H. J. Bolink, *Joule*, 2017, **1**, 431–442.
107 J. Xu, C. H. J. Moran, A. Ghorai, F. Bateni, J. A. Bennett, N. Mukhin, K. Latif, A. Cahn, P. Jha, F. D. Licona, S. Sadeghi, L. Politi and M. Abolhasani, *Nat. Commun.*, 2025, **16**, 7841.